Article

Motor neurons generate pose-targeted movements via proprioceptive sculpting

Check for updates

Benjamin Gorko[1,2], Igor Siwanowicz[1], Kari Close[1], Christina Christoforou[1], Karen L. Hibbard[1], Mayank Kabra[1], Allen Lee[1], Jin-Yong Park[1], Si Ying Li[1,3], Alex B. Chen[1,4], Shigehiro Namiki[1,5], Chenghao Chen[1,6], John C. Tuthill[6], Davi D. Bock[1,7], Hervé Rouault[1,8], Kristin Branson[1], Gudrun Ihrke[1] & Stephen J. Huston[1,9 ✉]

Motor neurons are the final common pathway[1] through which the brain controls movement of the body, forming the basic elements from which all movement is composed. Yet how a single motor neuron contributes to control during natural movement remains unclear. Here we anatomically and functionally characterize the individual roles of the motor neurons that control head movement in the fly, *Drosophila melanogaster*. Counterintuitively, we find that activity in a single motor neuron rotates the head in different directions, depending on the starting posture of the head, such that the head converges towards a pose determined by the identity of the stimulated motor neuron. A feedback model predicts that this convergent behaviour results from motor neuron drive interacting with proprioceptive feedback. We identify and genetically[2] suppress a single class of proprioceptive neuron[3] that changes the motor neuron-induced convergence as predicted by the feedback model. These data suggest a framework for how the brain controls movements: instead of directly generating movement in a given direction by activating a fixed set of motor neurons, the brain controls movements by adding bias to a continuing proprioceptive–motor loop.

To understand how the nervous system controls movements, it is necessary to understand the repertoire of motor neuron-driven movements available to the brain when choreographing the motion of the body. Any given motor neuron resides deep within a nested hierarchy of neural feedback loops[4,5] and can participate in many different movements in which its effects will vary, depending on the state of the rest of the motor system. Thus, a concise, interpretable, but still accurate description, of the movement generated by any given motor neuron remains a fundamental hurdle to understanding how the brain controls movement.

Drosophila offers an emerging platform in which single, identified neurons can be perturbed during behaviour, with the potential to create tools to do so for an entire motor subsystem[6–8]. Here we comprehensively analyse how the behavioural consequences of single motor neuron activation change across motor context. We perform this characterization for most of the motor neurons that control head position, revealing the contribution to behaviour of a population of the most fundamental motor elements of the nervous system.

## Neck motor neurons transform vision into movement

Many behaviours incorporate head movements, which in the fly are controlled by about 25 motor neurons driving small muscles in the neck[9,10] (Fig. 1a). Flies can rotate their head around all three cardinal axes (roll, pitch and yaw) and such movements are often visually driven. In particular, to stabilize its gaze, the fly must continuously adjust its head in response to visual motion[11,12]. To ascertain the role of an example neck motor neuron in controlling head movement in *Drosophila*, we first focused on the neck motor neuron CvN7 and investigated its potential role in gaze stabilization[9].

In flies, gaze stabilization uses a class of visual projection neurons, the lobula plate tangential cells[13,14] (LPTCs), which detect optic flow patterns resulting from particular axes of self-rotation[15]. To determine if LPTCs input directly to CvN7, we double-labelled LPTCs (magenta, Fig. 1b) and CvN7 (green, Fig. 1b). This showed that the visual neuron axons wrap around the dendrites of CvN7. Reconstruction of two motor neurons in the FAFB whole-brain electron microscopy dataset[16] (Extended Data Fig. 1) confirmed synaptic connectivity between five specific visual neurons in the larger bilateral LPTC population[14] and the motor neurons CvN6 and CvN7 (refs. 9,17) whose dendrites branch in both sides of the brain (inset, Fig. 1b and Extended Data Fig. 1). To determine the particular optic flow pattern that CvN7 is most responsive to, we performed patch clamp recordings during visual stimulus presentation. This showed that CvN7 responds to downward visual motion (Fig. 1c). Scanning small visual stimuli across the fly's visual field allows reconstruction of the visual receptive field of the motor neuron[15,18] (Fig. 1d), the structure of which suggests that the

[1]Janelia Research Campus, Howard Hughes Medical Institute, Ashburn, VA, USA. [2]Molecular, Cellular and Developmental Biology, University of California, Santa Barbara, CA, USA. [3]The Solomon H. Snyder Department of Neuroscience, Johns Hopkins University, Baltimore, MD, USA. [4]Program in Neuroscience, Harvard Medical School, Boston, MA, USA. [5]Research Center for Advanced Science and Technology, University of Tokyo, Tokyo, Japan. [6]Department of Physiology and Biophysics, University of Washington, Seattle, WA, USA. [7]Department of Neurological Sciences, University of Vermont, Burlington, VT, USA. [8]Turing Centre for Living systems, Aix-Marseille University, Université de Toulon, CNRS, CPT (UMR 7332), Marseille, France. [9]Mortimer B. Zuckerman Mind Brain Behavior Institute, Columbia University, New York, NY, USA. ✉e-mail: stephen.huston@columbia.edu
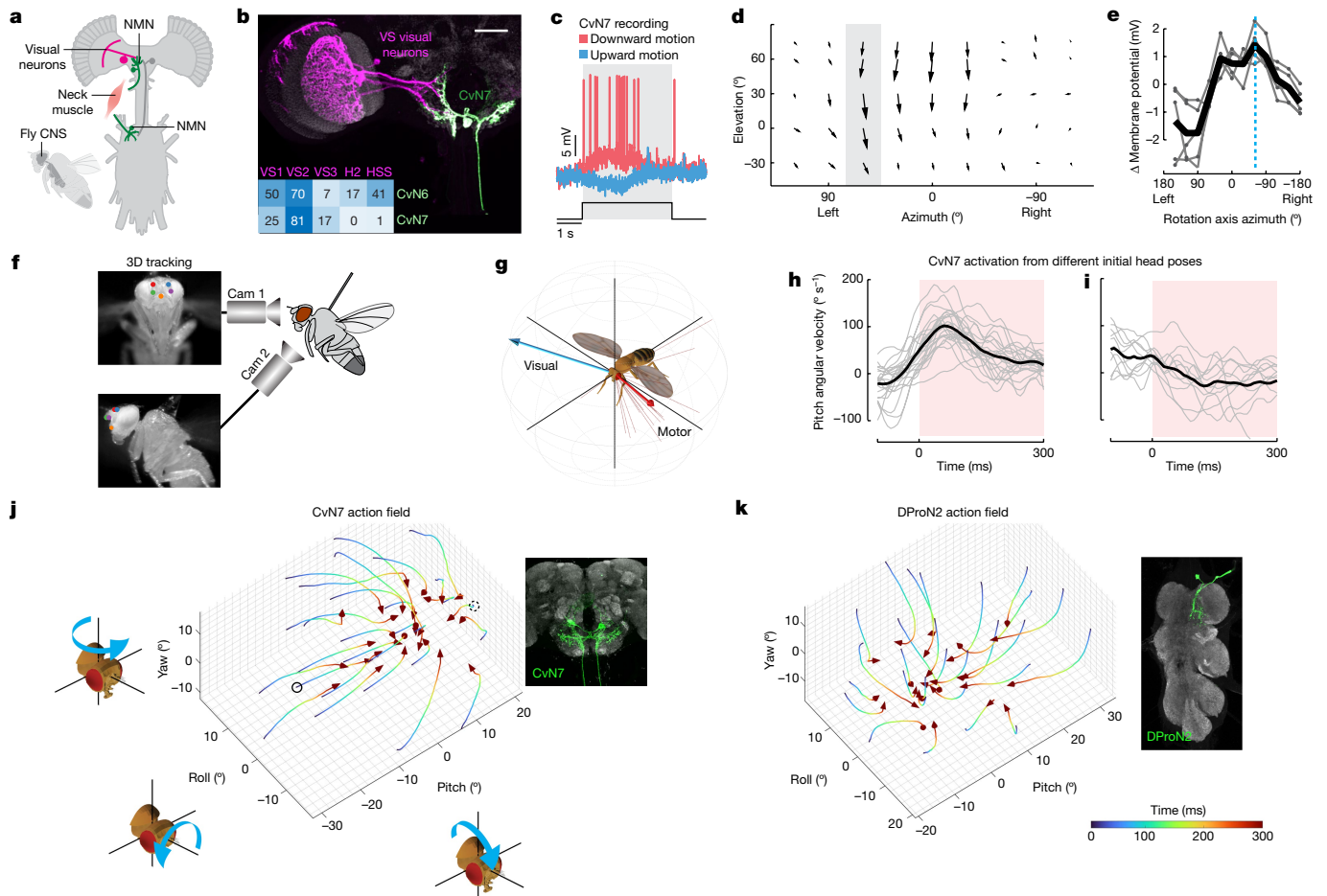
Fig. 1 | Motor neuron stimulation generates convergent movements.
a,**b**, Schematic (**a**) and confocal (**b**) image showing neck motor neuron dendrites (green) overlapping with LPTCs (magenta; scale bar, 50 μm). Subpanel, synapse counts between LPTCs and two neck motor neurons[14,16]. HSS is ipsilateral to the motor neuron axons, VS1–3 and H2 are contralateral. **c**, CvN7 responses to downward (red) or upward (blue) local visual motion. The upward response (blue) is time-reversed so each *x* axis location corresponds to the same portion of visual space for both traces. **d**, The visual receptive field of CvN7 (Methods). Black arrows indicate the preferred visual motion direction and response magnitude. Shaded region, data from **c**. **e**, The response of CvN7 to full-field visual rotation. Thin lines, individual trials (*n* = 5); thick line, mean. Dotted blue line, axis of rotation predicted from **d** to give the strongest response. **f**, Behavioural setup (Methods). Images are video frames taken simultaneously from two angles; coloured dots are 3D tracked points. **g**, Red arrow, grand

mean axis of head rotation following unilateral CvN7 stimulation; thin red lines, individual fly means. Blue arrow, axis of wide-field visual rotation that elicited the maximum response in **e**. **h**,**i**, Pitch movements induced by bilateral CvN7 stimulation with pitched-up (21 trials) (**h**) or pitched-down (11 trials) (**i**) starting postures. Grey lines, individual trials from several flies; black lines, mean; red region, stimulus. Positive angular velocity indicates downward head movement. **j**,**k**, The 'action fields' of two neurons (Methods), showing the average head rotation elicited during motor neuron activation at different starting postures. Data are plotted in 'quaternion space'[46], not Euler angles; Methods. Colour, time during stimulus. Inset, example image of neurons. **j**, Bilateral CvN7 (2,442 trials, 32 flies). Solid and dotted circles, starting postures of **h** and **i**, respectively. **k**, DproN2 (3,912 trials, 21 flies). CNS, central nervous system. NMN, neck motor neuron.

neuron should respond most strongly during pitch-up movements that result in downward visual motion across the retina[15]. To test this, we presented the fly with wide-field 'star field' stimuli and recorded the responses of the motor neuron as the star field was rotated around different axes (Fig. 1e). CvN7 responds most strongly to rotation of the visual world around the axis predicted from the piecewise receptive field mapping (Fig. 1e, dotted line is the axis predicted from the receptive field in 1d).

If CvN7 participates in gaze stabilization, it should, in response to the pitch-up motion it detects, drive pitch-down head rotations to stabilize the fly's gaze. We tested this by optogenetically stimulating CvN7 and measuring in three dimensions (3D) the resulting head movements (Fig. 1f). CvN7 activation pitches the head downward as predicted from its visual responses (Fig. 1g, mean axis of head rotation: 69° azimuth, 18° elevation with a spherical variance[19] of 0.09 where 0 indicates that all data are perfectly aligned and 1 indicates that the

data are distributed equally across the entire sphere). As in other fly species[18], *Drosophila* neck motor neurons are thus compactly transforming the visual consequences of the fly rotating in space into the appropriate counter-rotation of the head to stabilize the fly's gaze.

Motor neuron-induced movement is pose-dependent

Unexpectedly, the head rotations resulting from neck motor neuron stimulations were highly variable. Grouping CvN7-elicited movements by the initial posture of the head showed that the induced head rotations were highly dependent on the starting posture (Fig. 1h–j and Supplementary Videos 1 and 2). For example, when the head started in a pitched-up posture, stimulating the motor neuron-induced pitch-downward movements (Fig. 1h). However, when the head started in a pitched-down posture, activation of the same motor neuron induced much weaker movements in the opposite direction

Article

(Fig. 1i). To understand this posture dependence, we grouped trials with similar starting head postures and plotted the mean trajectory of the head for each group (Fig. 1j and Extended Data Fig. 2). We name such a plot the 'action field' of the motor neuron. For all starting postures, stimulating a given motor neuron caused the head posture to move towards a point of convergence in the action field (Fig. 1j). This means that stimulating the same motor neuron can lead the head to move in different directions, depending on starting posture. Which posture the head converges towards changed, depending on the identity of the motor neuron stimulated (Fig. 1k, single DproN2 motor neuron), in such a way to span the range of possible head movements (Supplementary Figs. 1–16).

Convergent movements resulting from microstimulation[20] have previously been attributed by some[21] to long and intense stimulation leading antagonistic muscles to be artificially co-activated. To test whether the convergent movements we observe are an artefact of our stimulus parameters, we tested the effect that length and intensity of stimulation had on the observed movement. We performed patch clamp recordings from the CvN7 motor neuron and identified stimulus intensities that spanned the range of action potential frequencies of the neuron (Extended Data Fig. 3). When using identical stimuli to activate CvN7 neurons in our behavioural experiments we observed convergent head movements, regardless of stimulus intensity (Extended Data Fig. 3). Increasing stimulus intensity does, however, increase the rotational velocity with which the head moves towards the convergence point (Extended Data Fig. 3). The convergence is not due to the head reaching the limit of its range of motion; the point of convergence of CvN7 is positioned 10–15° pitched down, whereas the head can pitch downward unimpeded as far as 35°. Restricting our analysis to only the first 80 ms of the stimulus period still shows convergent head movements (Extended Data Fig. 4). Similarly, excluding fast, saccadic movements of the head from our analysis or using a different head-fixed reference frame to measure rotations[22] still results in convergent head movements (Extended Data Fig. 4).

Feedback model captures pose-dependence

One potential explanation for the convergence behaviour is that the motor neuron stimulus is adding an offset to the control signal in a continuing feedback loop responsible for centring the head. To test for this, we computationally extracted an estimate of the stimulus-induced control signal from the recorded head movements. The plot in Fig. 2a shows the action field for CvN7. We generate an equivalent plot for control data, in which no stimulus was present and the head showed a tendency to return to its central position (Fig. 2b). For each time point of each trajectory in these plots, we compute the rotation required to transform the posture recorded in the control trajectory to the posture recorded at the same time in the matching stimulus trajectory. The resulting trajectories are plotted in Fig. 2c. These trajectories are approximately straight, reflecting a reduction in the correlation between head posture and stimulus-induced rotation (R^2 reduced from 0.45 to 0.22; Extended Data Fig. 2g). This analysis shows an approximately constant stimulus-induced offset which our optogenetic stimulus added to the head control feedback loop. The ability to extract this constant control signal from the curved and convergent head movements suggests that, although the head movement system is probably nonlinear, a linear feedback model may still be able to approximate a significant portion of the stimulus-induced behaviour.

On the basis of these results, we developed a linear feedback model in which motor neuron drive interacts with feedback carrying information about head position and velocity (Fig. 2d). The modelled head movement generated at any given time is proportional to the weighted sum of the external motor neuron stimulus and the current pose of the head (Fig. 2e). Thus, the convergent movements observed during motor neuron stimulation are modelled by the stimulus adding bias to a feedback loop that centres the head. The model was fit to half of our dataset and then used to simulate the other half without access to the data. The resulting simulated movements are qualitatively similar to the data, having the same convergent behaviour (compare Figs. 2f and 1j). The performance of the feedback model on simulating single trials was compared to that of a model without the feedback component, which reflects the more classical view that motor neurons generate the same movement independent of the animal's initial posture (Fig. 2g). The feedback model performs better at simulating individual trials, with a normalized root mean squared error (NRMSE) of 0.4 compared to the 0.6 of the feedforward model (Fig. 2i). An NRMSE value of zero means that the model predicted the trajectory of all individual trials perfectly and an NRMSE of one means that a model where the head does not move from its initial position would have performed better. Similarly, the proportion of trials where the error in the simulated head pose was below 5° is 71% compared to the 45% of the feedforward model (Fig. 2h).

Proprioception sculpts pose-dependence

The source of postural feedback predicted by our model could be of neural or biomechanical origin. To distinguish the relative contributions of these mechanisms we performed proprioceptive manipulations, which are unlikely to affect the biomechanics but will alter any neural mechanisms reliant on proprioceptive feedback.

To perturb specific subsets of proprioceptors and change the proprioceptive feedback in a targeted manner we generated two split-GAL4 lines. Each line expresses in a different subpopulation of proprioceptive sensory neurons that innervate the neck chordotonal organ. The neck chordotonal organ is a stretch-sensitive internal mechanoreceptor[9,23,24] strung parallel to the neck muscles by connective tissue (Fig. 3a–f and Extended Data Fig. 5). One sensory neuron type, which we call the lateral neck chordotonal neurons (LNCs), innervates the lateral side of the chordotonal organ (Fig. 3a–c). Another anatomically distinct sensory neuron type, which we call the medial neck chordotonal neurons (MNCs), innervates the far medial side of the organ (Fig. 3d–f). Both sensory neuron types project to the ventral nerve cord through the prothoracic nerve, where they travel through the dorsal medial tract and send process towards the midline (Fig. 3a,d and Extended Data Fig. 5).

If neural integration of proprioceptive feedback contributes to the convergence behaviour during motor neuron stimulation, then changing the proprioceptive feedback should change the action field of the motor neuron. We tested this hypothesis by perturbing the LNC proprioceptive neurons with Kir2.1-induced hyperpolarization during CvN7 stimulation (Fig. 3l). Our hypothesis predicts that this should change proprioceptive feedback to the entire neck motor system, making the system more permissive around the axis the LNCs monitor and hence making any CvN7-induced head movement stronger around this axis. As predicted, changing the proprioceptive feedback changes the motor neuron action field (compare Fig. 3g with 3k or Extended Data Fig. 5p with 5r). Specifically, the resulting head movements are, on average, faster around the pitch axis than for proprioceptor-intact flies (Fig. 3g,k and Extended Data Fig. 5u,v, median pitch velocity at peak: $34°\ s^{-1} \pm 43°$ median ± interquartile range for control flies, $60°\ s^{-1} \pm 66°$ for LNC-hyperpolarized flies, $P = 5 \times 10^{-4}$, $n = 43$, two-sample Kolmogorov–Smirnov test whether the per-fly peak pitch velocities for the two genotypes are from the same continuous distribution, median difference effect size: $21° \pm 13°\ s^{-1}$). As a result, the head overshoots the normal convergence point (12° pitch, measured by the starting posture that results in the smallest average head movement) of CvN7 and converges instead towards a more pitched pose (19° pitch). This suggests that the LNC proprioceptor neurons and their downstream circuit function to damp the pitch velocity of the head. Indeed, freeing different parameters of the previously fit feedback model one-by-one (Fig. 3n and Supplementary Methods) shows that the best fit to the
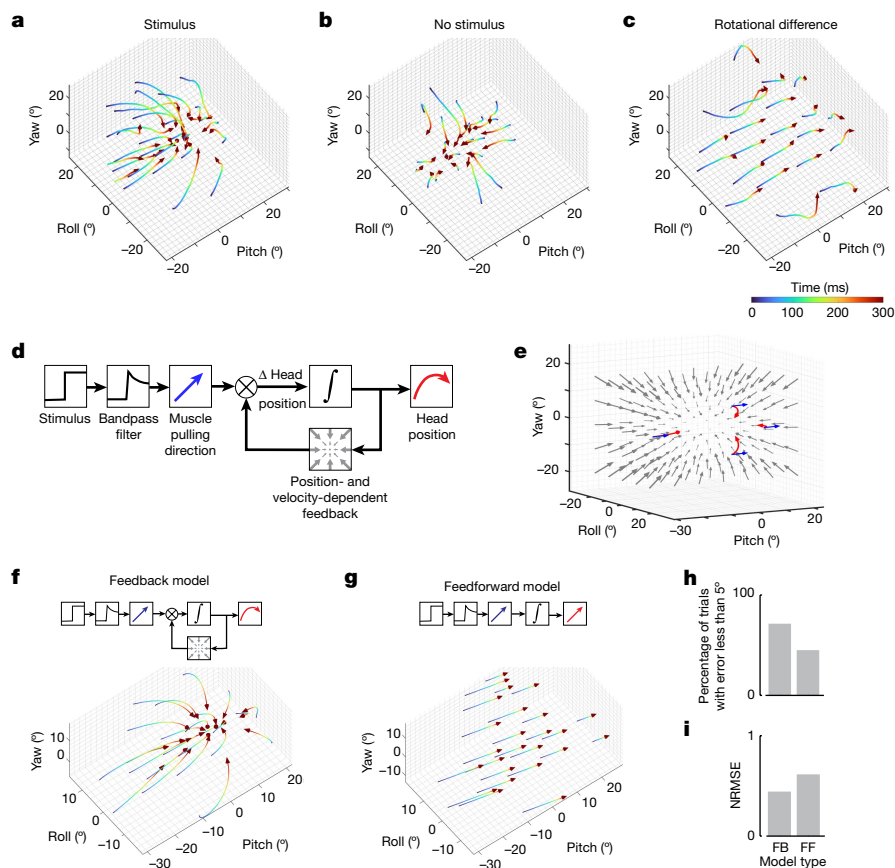
Fig. 2 | A feedback model explains the convergent movements elicited by motor neuron stimulation. a, The action field of the bilateral pair of CvN7 neurons (3,912 trials, 32 flies). **b**, The equivalent plot to **a** for a period of no stimulus (3,260 trials, 32 flies). **c**, The rotations required to transform each data point in **b** into its equivalent data point in **a**. **d**, The feedback model. The step-like optogenetic stimulus is bandpass filtered and drives a rotation of the head around a 3D axis (blue arrow). This drive is summed ($\otimes$) with the weighted 3D pose and velocity of the head. This results in the modelled net rotational change ($\varDelta$) in head position which is integrated ($\int$) to give the modelled head position (red arrow). **e**, An illustration of the effect on the model of the same motor neuron stimulus delivered at different starting head postures. Grey arrows plot the acceleration vector that the feedback loop

alone applies to the head (see Extended Data Fig. 5w for plot of velocity dependence). Blue arrows plot the acceleration component purely caused by the drive from the optogenetic stimulus. Red arrows plot the net head movement that occurs as a result of the interaction of the optogenetically driven activity (blue) and pose-dependent feedback (grey). **f**, The feedback model (FB) simulating held-out validation data. **g**, A feedforward (FF) model applied to the same data as in **f**. Any variance in trajectory length in **g** is due to variance in the data being simulated, not because of any postural dependence of the model. **h**, Percentage of simulated trials that predicted head poses within 5° of the actual head pose in the corresponding validation data. **i**, The NRMSE of the performance of each model (0, perfect match; 1, no better than model where head does not move).

LNC-hyperpolarized data is obtained by allowing the model parameter responsible for pitch velocity feedback to be reduced by 53% (Fig. 3m–o). In contrast to the strong effect observed during motor neuron stimulation, expressing Kir2.1 in the LNCs did not measurably affect the resting posture of the head, probably because the velocity damping performed by the LNCs falls outside the velocity range of normal head movements at rest (Extended Data Fig. 5t, two-sample Kolmogorov–Smirnov test whether the data are from the same continuous distribution: P = 0.3, 0.9 and 0.2 for roll, pitch and yaw, respectively, median difference effect sizes: 0.12°, 0.09°, −0.09°, n = 43 flies). Expressing Kir2.1 in either the MNCs or another neck proprioceptor, the prosternal organ[25], also changed the action field of CvN7 (Extended Data Fig. 5) but the effect could not be captured by changing a single parameter in our model.

A library of neck motor neuron types

We have found that stimulating a single motor neuron elicits convergent movements of the head which can be concisely described by its action field. To more fully characterize the motor system and determine if

this convergent behaviour was a general property of motor neurons, we measured action fields for most of the motor neurons innervating the neck motor system.

We constructed a library of genetic drivers (Extended Data Fig. 6 and Supplementary Table 1) which between them expressed in at least 16 of the about 25 pairs of motor neurons that drive fly head movements[10]. This is probably an undercount of the unique neuron types we performed experiments on, as some neurons could not be uniquely identified by their anatomy. For example, we could not separate the three VCvN motor neurons and so treat them as one class. We stochastically drove the optogenetic protein CsChrimson in single neurons from within the expression patterns of our genetic drivers and measured the head movements resulting from stimulating each neuron type. After the behavioural experiment we used confocal imaging of the same individual flies to identify the neurons that had been stimulated. Figure 4a,b shows the individually identified neurons we discovered. In addition, we obtained confocal images of the same neuron types in situ with the muscles still present to determine the structure of the neck motor system and identify which muscles each motor neuron innervates (Fig. 4c–h).
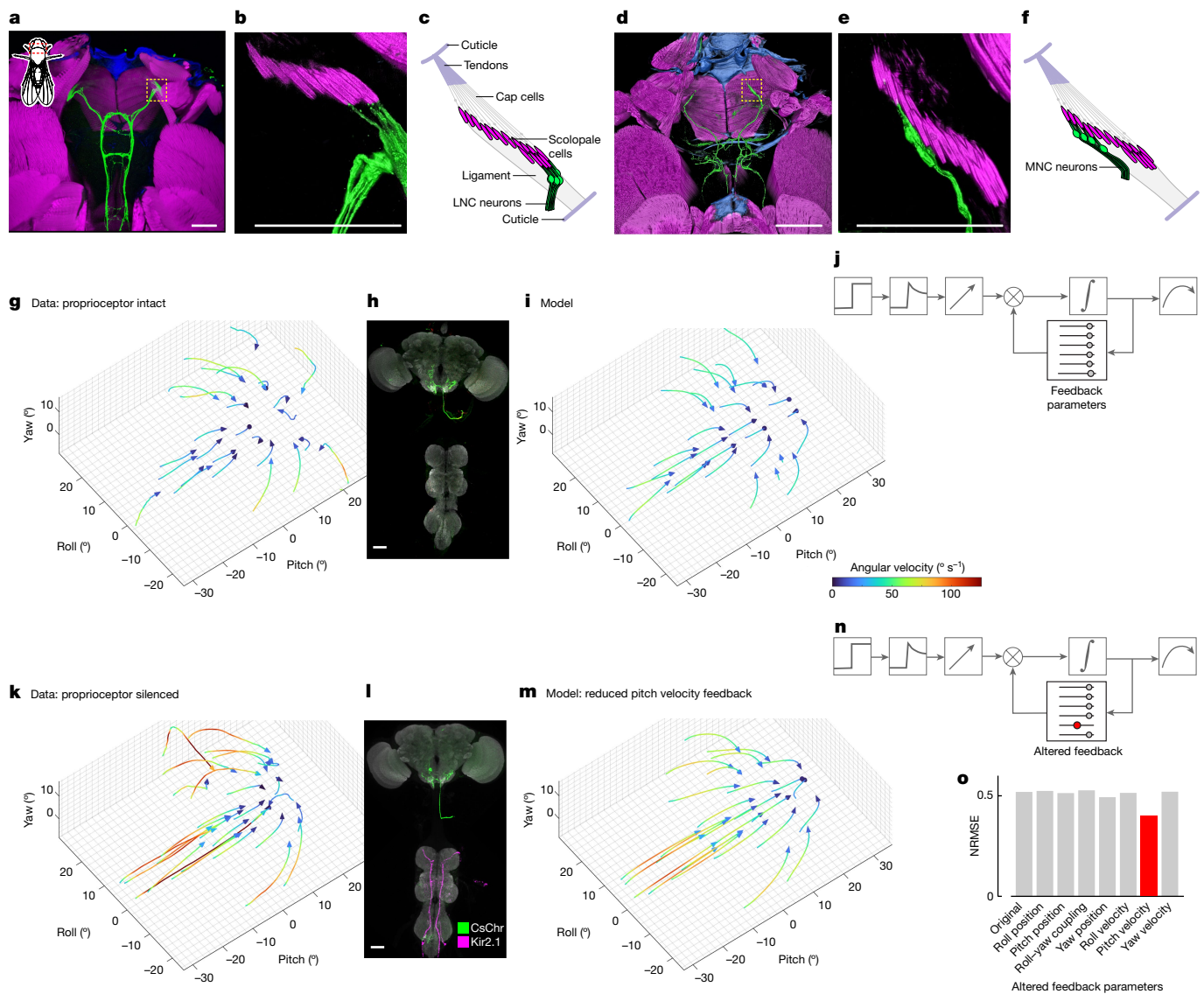
Fig. 3 | Silencing proprioceptors reshapes motor neuron-driven convergent movements. a–f, Anatomy of the neck chordotonal organ. **a**, Horizontal section of the anterior thorax, muscles shown in magenta (phalloidin), cuticle in blue (calcofluor white) and the LNCs in green (anti-GFP). **b**, Higher magnification of the highlighted region in **a**. **c**, Sensory LNC neuron dendrites insert into the centre of each scolopale (magenta tubes) on the lateral edge of the organ. **d**, Horizontal section of the anterior thorax, muscles shown in magenta (phalloidin), cuticle in blue (calcofluor white) and the MNCs in green (anti-GFP). **e**, Higher magnification of the highlighted region in **d**. **f**, MNC neuron dendrites innervate the scolopale cells at the medial edge of the chorodontonal organ. **g**, Action field of CvN7, colour-coded by angular velocity (35 flies, 2,132 trials). **h**, Example CNS of the genotype whose data is plotted in **g**. Green indicates

CsChrimson-mVenus expression in the CvN7 motor neuron. **i,j**, The results (**i**) of using a feedback model (**j**) to simulate the data in **g**. **k**, The action field of the same CvN7 neuron type when the LNC proprioceptive neurons are hyperpolarized (43 flies, 2,623 trials). **l**, Example CNS of the genotype whose data are plotted in **k**. Green indicates CsChrimson-mVenus expression in CvN7 neck motor neuron, magenta indicates Kir2.1::tdTomato expression in the LNC neurons and few unrelated abdominal neuromere neurons. **m**, The results (**m**) of using the feedback model with its pitch velocity feedback term reduced (**n**) to simulate the LNC-hyperpolarized data in **k**. **n,o**, The result of fitting each of the model parameters to the LNC-hyperpolarized data (Supplementary Methods). Two-dimensional versions of the plots in **g**–**m** are shown in Extended Data Fig. 5. Scale bars, 50 μm.

Anatomically, the motor neuron population falls into two groups: those whose cell bodies are in the brain and those in the ventral nerve cord. Neck motor neurons in the brain send axons posteriorly down the neck connective where they branch off to innervate muscles. Those neck motor neurons in the ventral nerve cord send axons anteriorly to the muscles either through nerves that leave the ventral nerve cord directly or by sending axons half way up the neck connective to then branch off (Fig. 4a,b and Extended Data Fig. 7). Most neck muscles do not directly enter the neck and are contained in the fly's thorax. These muscles control head movements either through long tendons that

travel through the neck to attach to the head directly or indirectly by moving the cervical sclerite: a triangular shaped, hardened cuticle segment in the thorax that comes to a point in the neck where it contacts the head[9] (Fig. 4g and Extended Data Fig. 7). The exceptions to this organization are three small oblique horizontal muscles whose tendons, unusually, do not attach directly to cuticle structures but instead fuse at a roughly 45° angle with the thick tendon of the much larger transverse horizontal muscle (Extended Data Fig. 8). Most muscles are innervated by a single motor neuron[9] (Fig. 4h) but many muscles have similar attachment points and therefore probably
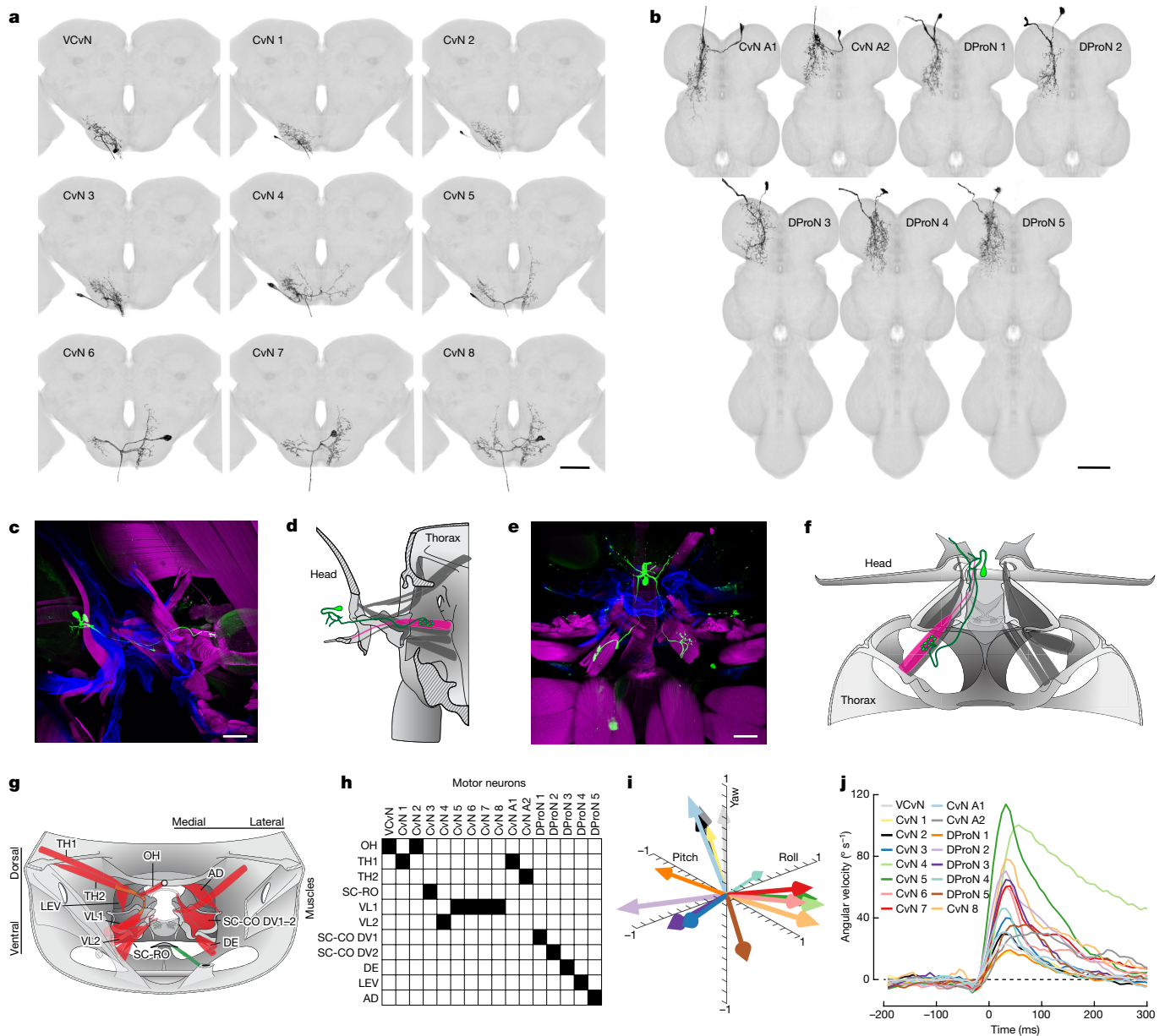
Fig. 4 | An anatomical and functional library of neck motor neurons.
a,**b**, Confocal images of neck motor neurons surveyed in this study whose cell bodies are in the brain (**a**) and ventral nerve cord (VNC) (**b**). Grey, standard brain/VNC template (male JRC2018[47]), which each image is aligned to[48]. Black, CsChrimson-mVenus expression in the neuron of interest. **c**,**d**, Side (sagittal plane) view confocal image (**c**) and diagram (**d**) of the CvN7 neck motor neuron in situ in the head (left), neck and thorax (right) of the body. The cell body of the motor neuron (green, anti-GFP) can be seen at the left of the image in the back of the fly's brain; its axon passes through the neck towards the thorax on the right of the image where it innervates the VL1 muscle (magenta, phalloidin), which moves the head by means of cuticular structures (blue, calcofluor white). **e**,**f**, The same as in **c** (**e**) and **d** (**f**) from an above (horizontal plane) view. Scale bars, 50 μm; colour-channel separated images available in Supplementary Fig. 17.

g, Diagram of all identified neck muscles; key muscle types labelled. View from inside the prothorax facing towards the neck. Red, muscle; orange, tendon; grey, cuticle; green, chordotonal organ. See Extended Data Fig. 7 for the complete set of muscle and cuticle structure labels. **h**, Motor neuron to muscle connectivity table (note that OH indicates a group of three muscles). See Extended Data Fig. 7 for all muscle name abbreviations. **i**, The mean axis of induced head rotation for each motor neuron. **j**, The speed of rotation around the mean axis of rotation of each motor neuron (those shown in **i**). See Supplementary Figs. 1–16 for number of trials and flies contributing to each trace in **i**,**j**. SC-CO DV, dorsoventral muscles linking the cervical sclerite and the condyle; VL, ventral longitudinal muscles; DE, depressor muscles; SC-RO, sclerite rotator muscle; LEV, levator muscle; TH, transverse horizontal muscles; OH, oblique horizontal muscles; AD, adductor muscle.

similar pulling planes. Figure 4h gives a summary of the motor neuron to muscle connectivity.

To generate a compact characterization of the function of each motor neuron and thus the whole neck motor system, we stimulated each neuron one-by-one and fit the feedback model to each set of generated movements (Supplementary Figs. 1–16). As with the CvN7 data, convergent movements were observed in most motor neurons and a feedback

model fit the data from all neuron types better than a feedforward one (mean NMSE 0.5 for the feedback model, 0.8 for the feedforward model) indicating that convergent movements are a general property of this motor neuron population. The axis each motor neuron rotates the head around is summarized in Fig. 4i and the speed of the induced head movement in Fig. 4j. The convergent action field of each motor neuron is shown in Supplementary Figs. 1–16.

Article

Discussion

Related work

Our data imply that motor commands from the brain cannot generate a fixed movement by always activating the same set of motor neurons. This is because the movement produced by motor neurons changes with posture. Instead, our data suggest that motor neuron inputs can control movement by adding bias to a continuing proprioceptive control loop. Similar, but distinct, ideas have been proposed previously as part of the 'equilibrium point hypothesis'[26,27] but have been contentious[28]. The equilibrium point hypothesis has two discrete components as follows. (1) That the combination of multimuscle biomechanics and spinal proprioceptive loops lead a limb to converge to a given posture and that this equilibrium posture can be changed by descending inputs altering the threshold to proprioceptive inputs of the spinal circuitry. (2) That the brain takes advantage of this convergence behaviour to specify desired movements as a sequence of such equilibrium points. Our data are consistent with the first part of the hypothesis. Indeed, previous work[29] on some fly neck motor neurons has found that descending input from the visual system alone does not lead to action potentials but instead changes the action potential threshold for mechanosensory inputs[29]. However, our data provide no evidence either way for the second part of the equilibrium point hypothesis. Rather than critically supporting the equilibrium point hypothesis, our data argue for the more general conclusion that the nervous system generates movement by changing ongoing control laws that govern the relationship between estimates of the state of the body and actual movements of the body[30,31]. This is probably a multilevel process consisting of several nested feedback loops[4,5] using different levels of abstraction in the estimate of the state of the body of which our direct proprioceptive–motor neuron loop is a low-level example.

Limitations

Our approach of stimulating individual motor neurons one-by-one relied on an assumption of pseudolinearity: that stimulating an individual motor neuron is informative about its role when acting in concert with others. This approach succeeded because we stimulated the same motor neuron many times during free behaviour, capturing and analysing its effects during many different movements and thus many different motor neuron population states. However, by definition, this approach will not capture nonlinear interactions between motor neurons. For example, we found that the tendons of the small oblique horizontal muscles fuse at an approximately 45° angle with the much larger transverse horizontal muscle tendon, possibly enabling the oblique horizontal muscles to adjust the line of action of the transverse horizontal muscle (Extended Data Fig. 8). This tendon fusion probably results in a nonlinear inter-reliance of the muscles which our analysis will not have captured[32,33].

For all single-neuron studies, the isolation of the influence of a single neuron is only an approximation; stimulating one neuron will in turn activate connected neurons. Studies in other species[17] have shown electrical synapses between synergistic motor neurons. Additionally, our analysis does not consider the temporal patterning of motor neuron activity[34].

Mechanism of convergence

In vertebrates, convergent force fields resulting from spinal stimulation are robust to proprioceptive de-afferentation[35] and are thought to be constructed by spinal interneurons indirectly engaging muscles with opposing viscoelastic properties[27]. Indeed, gross stimulation of vertebrate motor neuron pools did not result in convergent forces (after correction for forces at rest) as frequently as interneuron stimulation[36]. We have found that motor neurons produce convergent movements which change when a single subclass of proprioceptive neuron is perturbed. This suggests that one of the mechanisms underlying the convergence in our data is proprioceptive feedback. Proprioceptive feedback is, however, unlikely to be the only mechanism underlying the effects we observe; passive properties of the fly neck are likely to also contribute[37,38].

Functional role of convergence

In robotics, flexible movements have been achieved through dynamic movement primitives[39], where time-varying inputs modulate the behaviour of lower-level dynamical systems which behave similarly to the motor neuron-elicited movements reported here. These low-level dynamical systems ensure that the trajectory specified by their inputs reaches the desired target. Analogously, neuron–proprioceptor loops may transform descending motor commands into control laws useful for generating complex movements that are robust to perturbations.

Motor neurons driving convergent movements may be useful for behaviours where a stimulus triggers the adoption of a particular posture such as in grooming[40] or escape preparation[41]. However, many other behaviours require the generation of movements in a fixed direction, such as the control of head movements by the superior colliculus in mammals[42] or fly optomotor head movements (Fig. 1). In such systems, descending control from the brain must dynamically adjust with posture to account for the posture dependence of the downstream motor neurons[43–45]. In some cases, generating fixed motion in the relevant sensory reference frame may require convergent movements[22].

The motor system is able to produce flexible and diverse outputs because of the ability of the same motor neurons to contribute in different ways to many different movements. Because of this multifunctionality it has been challenging to obtain a condensed, interpretable description of the output of a motor neuron that also captures its changing roles across different movements. Here, we obtain such a condensed description of motor neuron output for a population of motor neurons. This description paves the way for understanding how the descending control of movement interfaces with a dynamic motor system.

Online content

Any methods, additional references, Nature Portfolio reporting summaries, source data, extended data, supplementary information, acknowledgements, peer review information; details of author contributions and competing interests; and statements of data and code availability are available at https://doi.org/10.1038/s41586-024-07222-5.

1. Sherrington, C. *The Integrative Action of the Nervous System* (Cambridge Univ. Press Archive, 1952).
2. Dionne, H., Hibbard, K. L., Cavallaro, A., Kao, J.-C. & Rubin, G. M. Genetic reagents for making Split-GAL4 lines in *Drosophila*. *Genetics* **209**, 31–35 (2018).
3. Milde, J. J., Seyan, H. S. & Strausfeld, N. J. The neck motor system of the fly *Calliphora erythrocephala*. II Sensory organization. *J. Comp. Physiol. A* **160**, 225–238 (1987).
4. Merel, J., Botvinick, M. & Wayne, G. Hierarchical motor control in mammals and machines. *Nat. Commun.* **10**, 5489 (2019).
5. Scott, S. H. A functional taxonomy of bottom-up sensory feedback processing for motor actions. *Trends Neurosci.* **39**, 512–526 (2016).
6. McKellar, C. E., Siwanowicz, I., Dickson, B. J. & Simpson, J. H. Controlling motor neurons of every muscle for fly proboscis reaching. *eLife* **9**, e54978 (2020).
7. Baek, M. & Mann, R. S. Lineage and birth date specify motor neuron targeting and dendritic architecture in adult *Drosophila*. *J. Neurosci.* **29**, 6904–6916 (2009).
8. Azevedo, A. W. et al. A size principle for recruitment of *Drosophila* leg motor neurons. *eLife* **9**, e56754 (2020).
9. Strausfeld, N. J., Seyan, H. S. & Milde, J. J. The neck motor system of the fly *Calliphora erythrocephala*. I Muscles and motor neurons. *J. Comp. Physiol. A* **160**, 205–224 (1987).
10. Phelps, J. S. et al. Reconstruction of motor control circuits in adult *Drosophila* using automated transmission electron microscopy. *Cell* **184**, 759–774 (2021).
11. Hengstenberg, R. Gaze control in the blowfly *Calliphora*: a multisensory, two-stage integration process. *Semin. Neurosci.* **3**, 19–29 (1991).
12. Kim, A. J., Fenk, L. M., Lyu, C. & Maimon, G. Quantitative predictions orchestrate visual signaling in *Drosophila*. *Cell* **168**, 280–294 (2017).
13. Borst, A., Haag, J. & Reiff, D. F. Fly motion vision. *Annu. Rev. Neurosci.* **33**, 49–70 (2010).
14. Zhao, A. et al. A comprehensive neuroanatomical survey of the *Drosophila* lobula plate tangential neurons with predictions for their optic flow sensitivity. *eLife* **13**, RP93659 (2024).
15. Krapp, H. G. & Hengstenberg, R. Estimation of self-motion by optic flow processing in single visual interneurons. *Nature* **384**, 463–466 (1996).

16. Zheng, Z. et al. A complete electron microscopy volume of the brain of adult *Drosophila melanogaster*. *Cell* **174**, 730–743 (2018).
17. Wertz, A., Haag, J. & Borst, A. Integration of binocular optic flow in cervical neck motor neurons of the fly. *J. Comp. Physiol. A* **198**, 655–668 (2012).
18. Huston, S. J. & Krapp, H. G. Visuomotor transformation in the fly gaze stabilization system. *PLoS Biol.* **6**, e173 (2008).
19. Fisher, N. I. *Statistical Analysis of Circular Data* (Cambridge Univ. Press, 1993).
20. Graziano, M. S. A., Taylor, C. S. R. & Moore, T. Complex movements evoked by microstimulation of precentral cortex. *Neuron* **34**, 841–851 (2002).
21. Griffin, D. M., Hudson, H. M., Belhaj-Saïf, A. & Cheney, P. D. EMG activation patterns associated with high frequency, long-duration intracortical microstimulation of primary motor cortex. *J. Neurosci.* **34**, 1647–1656 (2014).
22. Klier, E. M., Wang, H. & Crawford, J. D. The superior colliculus encodes gaze commands in retinal coordinates. *Nat. Neurosci.* **4**, 627–632 (2001).
23. Field, L. H. & Matheson, T. Chordotonal organs of insects. *Adv. Insect Physiol.* **27**, 1–228 (1998).
24. Tuthill, J. C. & Azim, E. Proprioception. *Curr. Biol.* **28**, R194–R203 (2018).
25. Preuss, T. & Hengstenberg, R. Structure and kinematics of the prosternal organs and their influence on head position in the blowfly *Calliphora erythrocephala*. *J. Comp. Physiol. A* **171**, 483–493 (1992).
26. Feldman, A. G. Functional tuning of the nervous system with control of movement or maintenance of a steady posture. II. Controllable parameters of the muscle. *Biofizika* **11**, 565–578 (1966).
27. Bizzi, E., Mussa-Ivaldi, F. A. & Giszter, S. Computations underlying the execution of movement: a biological perspective. *Science* **253**, 287–291 (1991).
28. Sainburg, R. L. Should the equilibrium point hypothesis (EPH) be considered a scientific theory? *Motor Control* **19**, 142–148 (2015).
29. Huston, S. J. & Krapp, H. G. Nonlinear integration of visual and haltere inputs in fly neck motor neurons. *J. Neurosci.* **29**, 13097–13105 (2009).
30. Todorov, E. & Jordan, M. I. Optimal feedback control as a theory of motor coordination. *Nat. Neurosci.* **5**, 1226–1235 (2002).
31. Shadmehr, R. From equilibrium point to optimal control. *Motor Control* **14**, e25–e30 (2010).
32. Gorb, S. N. The jumping mechanism of cicada *Cercopis vulnerata* (Auchenorrhyncha, Cercopidae): skeleton–muscle organisation, frictional surfaces and inverse-kinematic model of leg movements. *Arthropod Struct. Dev.* **33**, 201–220 (2004).
33. Siwanowicz, I. & Burrows, M. Three dimensional reconstruction of energy stores for jumping in planthoppers and froghoppers from confocal laser scanning microscopy. *eLife* **6**, e23824 (2017).
34. Sober, S. J., Sponberg, S., Nemenman, I. & Ting, L. H. Millisecond spike timing codes for motor control. *Trends Neurosci.* **41**, 644–648 (2018).
35. Loeb, E. P., Giszter, S. F., Borghesani, P. & Bizzi, E. Effects of dorsal root cut on the forces evoked by spinal microstimulation in the spinalized frog. *Somatosens. Mot. Res.* **10**, 81–95 (1993).
36. Caggiano, V., Cheung, V. C. K. & Bizzi, E. An optogenetic demonstration of motor modularity in the mammalian spinal cord. *Sci. Rep.* **6**, 35185 (2016).
37. Gilbert, C. & Bauer, E. Resistance reflex that maintains upright head posture in the flesh fly *Neobellieria bullata* (Sarcophagidae). *J. Exp. Biol.* **201**, 2735–2744 (1998).
38. Cellini, B., Salem, W. & Mongeau, J.-M. Mechanisms of punctuated vision in fly flight. *Curr. Biol.* **31**, 4009–4024 (2021).
39. Ijspeert, A., Nakanishi, J. & Schaal, S. Learning attractor landscapes for learning motor primitives. *Adv. Neural Inf. Process. Syst.* **15**, 1547–1554 (2002).
40. Durr, V. & Matheson, T. Graded limb targeting in an insect is caused by the shift of a single movement pattern. *J. Neurophysiol.* **90**, 1754–1765 (2003).
41. Card, G. & Dickinson, M. H. Visually mediated motor planning in the escape response of *Drosophila*. *Curr. Biol.* **18**, 1300–1307 (2008).
42. Masullo, L. et al. Genetically defined functional modules for spatial orienting in the mouse superior colliculus. *Curr. Biol.* **29**, 2892–2904 (2019).
43. Wolpert, D. M. & Ghahramani, Z. Computational principles of movement neuroscience. *Nat. Neurosci.* **3**, 1212–1217 (2000).
44. Fujiwara, T., Brotas, M. & Chiappe, M. E. Walking strides direct rapid and flexible recruitment of visual circuits for course control in *Drosophila*. *Neuron* **110**, 2124–2138 (2022).
45. Cruz, T. L., Pérez, S. M. & Chiappe, M. E. Fast tuning of posture control by visual feedback underlies gaze stabilization in walking *Drosophila*. *Curr. Biol.* **31**, 4596–4607 (2021).
46. Tweed, D., Cadera, W. & Vilis, T. Computing three-dimensional eye position quaternions and eye velocity from search coil signals. *Vision Res.* **30**, 97–110 (1990).
47. Bogovic, J. A. et al. An unbiased template of the *Drosophila* brain and ventral nerve cord. *PLoS ONE* **15**, e0236495 (2020).
48. Rokicki, K. et al. Janelia workstation codebase. *GitHub* https://github.com/JaneliaSciComp/workstation (2019).

Article

Methods

Generation of genetic lines

Genetic lines were generated that expressed in sparse subsets of one to ten neck motor neurons by using the split-GAL4 technique[49,50] to generate intersections from published hemidrivers[2,51].

For most motor neurons, it is necessary to activate only a single neuron out of each bilateral pair expressed by the split-GAL4 line to ensure that the innervated muscles of the two neurons do not oppose each other. For example, in the case of a yaw-inducing motor neuron, the left and right neurons of the bilateral pair will drive the head to move in opposite directions making interpretation of the movement induced by bilateral stimulation challenging. In the special case of pitch-inducing motor neurons, for example CvN7, unilateral stimulation is not necessary as both motor neurons in the bilateral pair drive the same pitch movements. Accordingly, for CvN7 we used genotypes that only expressed in one unilateral neuron or both bilateral neurons as the experimental constraints demanded. For all other motor neurons, we only performed unilateral simulation. To achieve expression of the optogenetic protein CsChrimson[52] in single motor neurons we stochastically expressed it in each of the split-GAL4 lines (Supplementary Methods). Flies were dissected after the behavioural experiments to identify the motor neuron expressing CsChrimson. Flies that did not express CsChrimson in any neurons served as genetically identical controls. To determine the effect of silencing proprioceptors on motor neuron-elicited movements, we used similar fly lines but with the CsChrimson driven by a sparse LexA driver that expressed in CvN7 and proprioceptor-specific split-GAL4 lines expressing Kir2.1 in specific subsets of neck proprioceptive neurons. See Supplementary Methods, Extended Data Table 1 and Supplementary Table 1 for details of genotypes and protocols. See Supplementary Table 2 for details of neurons identified in electron microscopy connectome datasets.

Behavioural experiment pipeline

Tethered, flying flies were videoed from two orthogonal angles at 125 frames per second while presenting 300 ms flashes of red light (625 nm, 0.37 mW mm^{-2}) spaced 1.5 s apart for a total of 120 flashes. Owing to the presence of a loss-of-function allele of *norpA*[53], flies were blind and did not show any behavioural reaction to the red light stimulus. The resulting videos were then tracked in 3D[54]. Flies were individually dissected, subject to direct-label immunohistochemistry and imaged using confocal microscopy while keeping track of fly identity. This enabled us to determine which neurons were optogenetically activated in each fly. See Supplementary Methods for details of histology and imaging.

Head tracking

To track head movements we used the animal part tracker[54] to track five points on the fly head. We tracked these landmarks in two dimensions using a custom deep learning-based network (Supplementary Methods) and then combining these estimates to generate a 3D estimate of their position. The resulting set of 3D points are rotated so that the hand-annotated 3D body axis is aligned across all flies and the origin sits in the neck at the computationally estimated pivot point. The data are presented rotated so that the body axis is pitched upwards 40° relative to the horizon in approximately the posture seen during *Drosophila* flight. The 3D rotations between frames are then calculated from the tracked points using Horn's method[55]. The global, laboratory frame coordinate conventions used are described in Extended Data Fig. 2c.

Action field plots

To visualize how the movements induced by single-neuron activation change with time and posture we plot 'action fields' for each neuron, for example Fig. 1j. The head rotations from individual motor neuron stimulation trials were grouped into bins[56] according to the starting posture of the head in the frame before the stimulus started. We plot the average[57] rotation trajectory of each group, colour-coded by time or rotational velocity. The position in the three axes describes the 3D rotational pose of the head at any given time. The three axes of the plot are labelled roll, pitch and yaw but are not Euler angles; instead, they plot the 3D axis of rotation scaled by the magnitude of the same rotation[46]. Thus, the data are plotted in what has previously been termed 'quaternion space'[46]: the axis the head is rotated about relative to its normal resting position determines in which 3D direction the point is plotted; the magnitude of the rotation determines how far from the origin the point is plotted along that direction. No interpolation is performed on these data.

Electrophysiology

To both measure the visual responses of a motor neuron (Fig. 1c−e) and also to calibrate the optogenetic stimulus (Extended Data Fig. 3) we performed patch clamp recordings from the CvN7 motor neuron using previously described methods[58] (Supplementary Methods). The optic fibre was placed in a similar location and distance relative to the neck as in the behavioural experiments and the same stimulus sequence delivered as in the behavioural experiments while monitoring the spike rate of CvN7.

Visual stimuli

The fly head was placed in between three orthogonal projector screens that formed the corner of a cube. Stimuli were corrected in OpenGL for perspective and individually measured head angle to appear as if stimuli were on the sphere surrounding the fly. Data are presented for motor neurons whose axon exits the nervous system on the right-hand side of the fly. Data from motor neurons with axons that exited through a nerve on the left side of the fly are flipped to appear as if they came from the equivalent neuron on the right side of the fly.

Visual receptive fields were mapped by scanning a 5° circular black target at 50° s^{-1} in the four cardinal directions across a grid that covered the virtual sphere surrounding the fly[59]. The responses of the neuron to wide-field rotation were measured by rotating a panoramic 'star field' stimulus around different axes relative to the fly.

Modelling head movements

The head movements induced by single motor neuron stimulation were modelled with a linear time invariant model. In this model, the head acceleration at any given time is proportional to the weighted sum of a motor neuron-specific 3D vector and feedback which is dependent on the current head position and velocity (Fig. 2d,e). The bandpass filtered LED stimulus r (Supplementary Methods) is multiplied by the simulated direction of pull $[m_x, m_y, m_z]$ of the motor neuron in the quaternion space representation[46] and linearly combined with a weighted sum of the current head posture and velocity to model any pose-dependent feedback. This sum determines the acceleration of the modelled head in the x, y and z dimensions of the modelled action field according to:

$$\ddot{x} = rm_x + xp_{11} + \dot{x}p_{14}$$

$$\ddot{y} = rm_y + yp_{22} + \dot{y}p_{25} + zp_{23}$$

$$\ddot{z} = rm_z + zp_{33} + \dot{z}p_{36}$$

$$p_{23} = \begin{cases} -p_{23}, & z_0 < 0 \\ p_{23}, & z_0 \geq 0 \end{cases}$$

where $x, y, z, \dot{x}, \dot{y}, \dot{z}$ are the current position and velocity of the head in the action field 3D representation of rotational pose and $p_{i,j}$ are the weights applied to the current position and velocity of the head. The feedforward model was the same as the above, except the feedback

parameters $p_{i,j}$ were all set to zero. See Supplementary Methods for details of the model, fitting and simulation. Model performance was measured in two different ways. The NRMSE was computed between the simulated and real individual trials over the entire 300 ms simulated period. The NRMSE was computed as:

$$\text{NRMSE} = \frac{\|\text{data} - \text{model}\|}{\|\text{data} - \text{mean}(\text{data})\|}$$

An NRMSE value of zero means the simulation was a perfect match to the validation data; an NRMSE value of one means the simulation performed no better than one in which the head does not move from its starting posture. The angular error was also computed for each frame of the validation data. The rotation required to align the simulated head pose with the actual head pose was calculated for each frame and averaged across the entire trial. We report the fraction of trials where this average angular error was less than 5°.

Reporting summary

Further information on research design is available in the Nature Portfolio Reporting Summary linked to this article.

Data availability

Data to reproduce the figures in this paper are available at bitbucket. org/stephenhuston/code_data_gorko_et_al. The expression patterns and flies for split-GAL4 lines generated in this study are available online at splitgal4.janelia.org (release: 'Gorko et al 2024'), except for JR153 and JR161 whose expression patterns can be downloaded at bitbucket.org/stephenhuston/code_data_gorko_et_al; flies available upon request. Electron microscopy data are available at fafb.catmaid. virtualflybrain.org (SKIDs: 1167858 (CvN6) and 1337777 (CvN7)).

Code availability

Code to reproduce the figures in this paper is available at bitbucket. org/stephenhuston/code_data_gorko_et_al.

49. Luan, H., Peabody, N. C., Vinson, C. R. & White, B. H. Refined spatial manipulation of neuronal function by combinatorial restriction of transgene expression. *Neuron* **52**, 425–436 (2006).
50. Pfeiffer, B. D. et al. Refinement of tools for targeted gene expression in *Drosophila*. *Genetics* **186**, 735–755 (2010).
51. Tirian, L. & Dickson, B. J. The VT GAL4, LexA and split-GAL4 driver line collections for targeted expression in the *Drosophila* nervous system. Preprint at *bioRxiv* https://doi.org/10.1101/198648 (2017).
52. Klapoetke, N. C. et al. Independent optical excitation of distinct neural populations. *Nat. Methods* **11**, 338–346 (2014).
53. Bloomquist, B. T. et al. Isolation of a putative phospholipase C gene of *Drosophila*, *norpA* and its role in phototransduction. *Cell* **54**, 723–733 (1988).
54. Lee, A., Kabra, M., Branson, K., Robie, A. A. & Roian, E. APT: animal part tracker. *GitHub* https://github.com/kristinbranson/APT (2018).
55. Horn, B. K. P. Closed-form solution of absolute orientation using unit quaternions. *J. Opt. Soc. Am. A* **4**, 629 (1987).
56. Yershova, A., Jain, S., Lavalle, S. M. & Mitchell, J. C. Generating uniform incremental grids on SO(3) using the Hopf fibration. *Int. J. Rob. Res.* **29**, 801–812 (2010).
57. Markley, F. L., Cheng, Y., Crassidis, J. L. & Oshman, Y. Averaging quaternions. *J. Guid. Control Dynam.* **30**, 1193–1197 (2007).
58. Maimon, G., Straw, A. D. & Dickinson, M. H. Active flight increases the gain of visual motion processing in *Drosophila*. *Nat. Neurosci.* **13**, 393–399 (2010).
59. Nordström, K., Barnett, P. D., de Miguel, I. M. M., Brinkworth, R. S. A. & O'Carroll, D. C. Sexual dimorphism in the hoverfly motion vision pathway. *Curr. Biol.* **18**, 661–667 (2008).
60. Nern, A., Pfeiffer, B. D. & Rubin, G. M. Optimized tools for multicolor stochastic labeling reveal diverse stereotyped cell arrangements in the fly visual system. *Proc. Natl Acad. Sci. USA* **112**, E2967–E2976 (2015).

Article

CvN 6: Light Microscopy

b
CvN 6: Electron Microscopy

c
CvN 7: Light Microscopy

d
CvN 7: Electron Microscopy

Extended Data Fig. 1 | Comparison of light and electron microscopy images of two neck motor neurons. (a-b) Comparison of light microscopy data (a) and electron microscopy (b) data for the CvN6 neck motor neuron. (a) Confocal image of CvN6. Grey = JRC2018 male standard brain template which the confocal image of the BRP neuropil stain was aligned to[47,48]. Black = CsChrimson-mVenus expression in CvN6. Scale bar = 50 μm. (b) Skeleton of the manually traced and proofread same CvN6 neuron in the FAFB whole-brain Electron Microscopy volume[16] (catmaid-fafb.virtualflybrain.org, SKID: 1167858). (c) Confocal image of CvN7, colours as for (a). (d) Skeleton of the manually traced and proofread same CvN7 neuron in the FAFB whole-brain Electron Microscopy volume (SKID: 1337777). Posterior and lateral views are shown for each dataset.
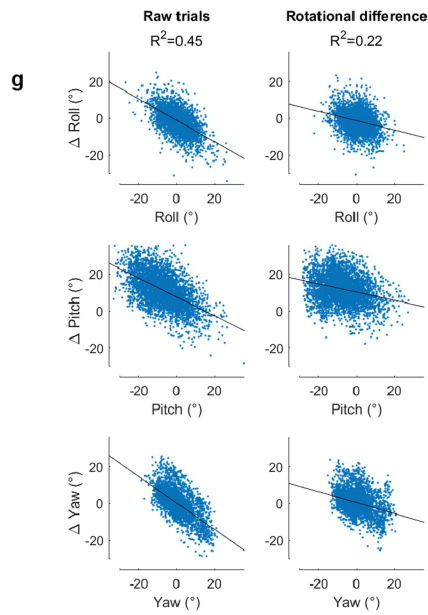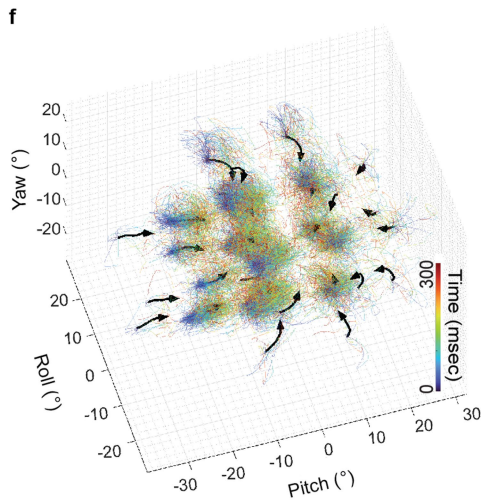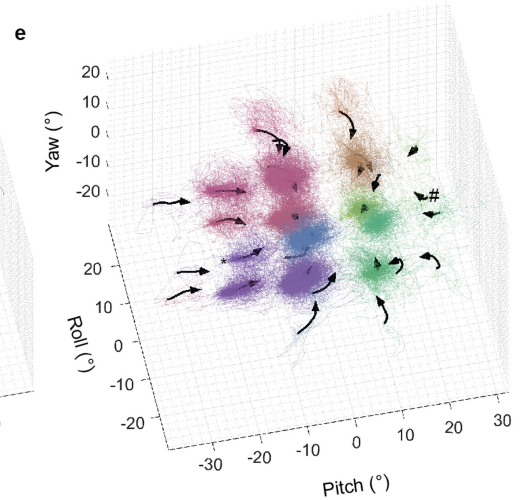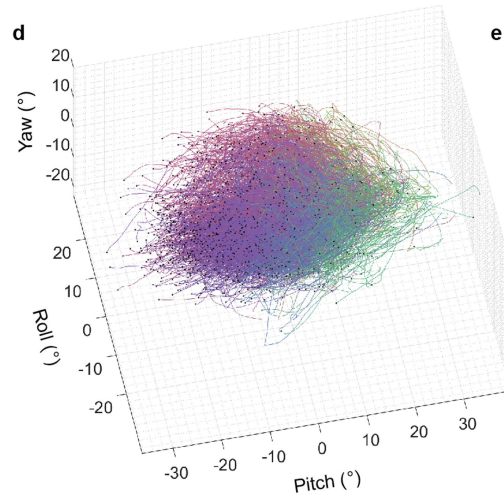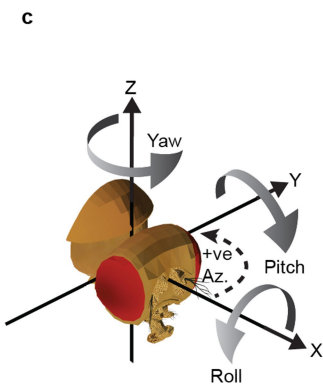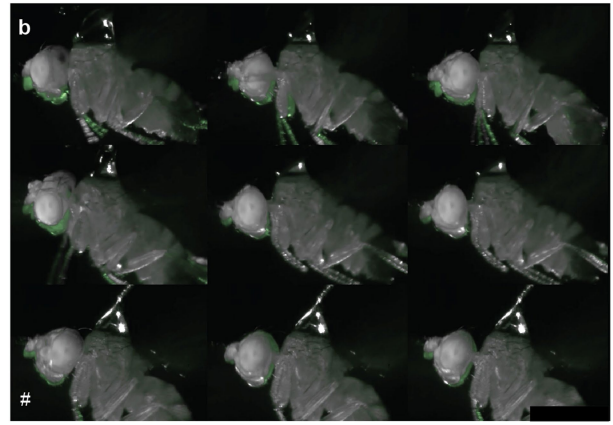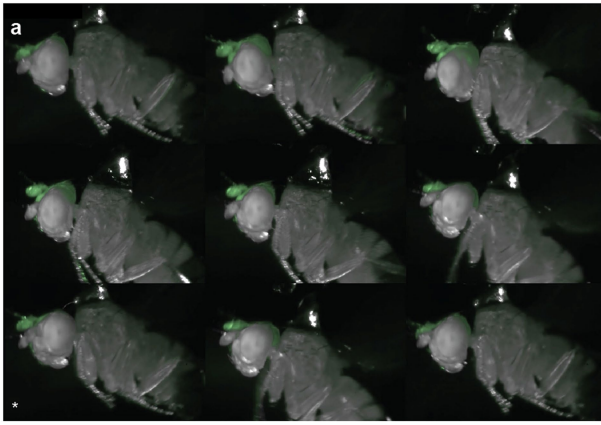
Extended Data Fig. 2 | See next page for caption.

Article

Extended Data Fig. 2 | Individual trial data used to generate CvN7 action fields. (a) Video frames of nine flies receiving a CvN7 stimulus when their head is initially pitched upward. The grayscale video frame is taken at the end of the 300 millisecond stimulus period, while the underlaid green image is from one frame before the stimulus started. The difference between the two frames illustrates the pitch downward head movement elicited by the CvN7 stimulus when the head 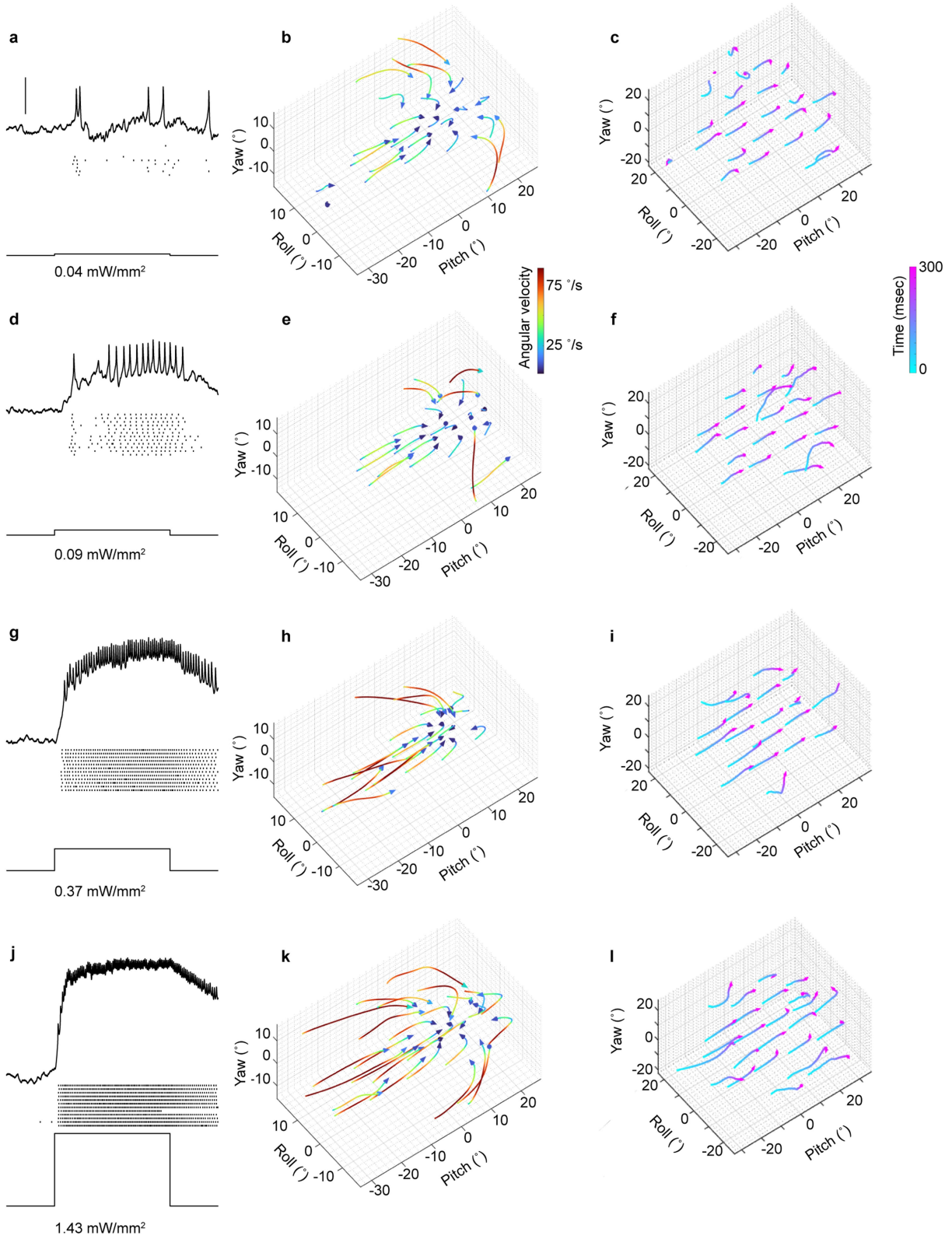starts in an upward posture. (b) Similar to panel a, this panel displays video frames of nine flies of the same genotype, but with the stimulus occurring when their heads were initially pitched downward. The difference between the overlaid grey (end of stimulus period) and green (before stimulus) frames illustrates the small pitch upward movement of the head elicited by the same CvN7 stimulus as in panel a. Symbols in the lower left hand corners of a & b correspond to the same symbols in panel e and indicate which data bins the videos frames were drawn from. See Supplementary Videos 1-2 for the source videos. (c) Coordinate system used in this paper. All head movement data (except Extended Data Fig. 4e,f) in this paper are presented in the global, lab-fixed frame coordinate system convention shown here. The X, Y and Z axis show the axes roll, pitch and yaw occur about respectively according to the right-hand rule. The origin is in the fly's neck, located at the computationally estimated pivot point of the head. The X axis is defined as tilted downward 40° from the tethered fly's long body axis, reflecting the resting head posture of a typical fly during flight. For plots of the visual responses of motor neurons we define positive elevation as moving upward from the X to the Z axis and positive azimuth as moving from the fly's front to its left, i.e. from the X axis to the Y axis. This azimuth/elevation convention is chosen to be consistent with our right-hand coordinate system for describing rotations of the head, but it does not match that previously used in the literature for describing visual receptive fields[15]. (d) The rotational trajectories of the head for all 2442 trials (32 flies) that were used to generate the CvN7 action field shown in Fig. 1j. Each line represents the trajectory of rotational postures occurring during one stimulation trial, with black dots indicating the head's starting posture. The colour of the lines corresponds to the starting posture and the axes are as in Fig. 1j. (e) The same data as in panel d, but with the trajectories grouped by the starting posture bin they were assigned to when generating the average trajectories plotted in Fig. 1j. The locations of the starting posture bins have been expanded by a factor of x3.5, moving them apart to prevent the data groups from obscuring each other. Black arrows indicate the quaternion averages of each bin. (f) The same plot as panel e but with the individual trajectories colour-coded by time since the stimulus was turned on. (g) depicts the relationship between the initial head posture and the CvN7 stimulus-induced change in head posture, using the individual trials underlying the means shown in Fig. 2a&c. The first column represents data from 3912 individual trials, illustrating the association between the head posture recorded just before stimulus onset and the subsequent change in head posture between the first and last frame of the stimulus. In the second column, we employ the additional processing step depicted in Fig. 2c. This involves calculating the 'rotational difference' between the no-stimulus and stimulus conditions. Specifically, we plot the rotations required to align each frame's head posture with the corresponding frame of the mean no-stimulus trajectory from the closest bin (depicted in Fig. 2b). In agreement with the mean data displayed in Fig. 2a–c, individual trials exhibit a correlation between initial head posture and stimulus-induced movement (first column, $R^2 = 0.45$). However, when plotting the 'rotational difference' between stimulus and no-stimulus conditions (second column), this correlation is reduced ($R^2 = 0.22$).

a

0.04 mW/mm²

b

Yaw (°), Roll (°), Pitch (°)

c

Yaw (°), Roll (°), Pitch (°)

Angular velocity
75 °/s
25 °/s

Time (msec)
300
0

d

0.09 mW/mm²

e

Yaw (°), Roll (°), Pitch (°)

f

Yaw (°), Roll (°), Pitch (°)

g

0.37 mW/mm²

h

Yaw (°), Roll (°), Pitch (°)

i

Yaw (°), Roll (°), Pitch (°)

j

1.43 mW/mm²

k

Yaw (°), Roll (°), Pitch (°)
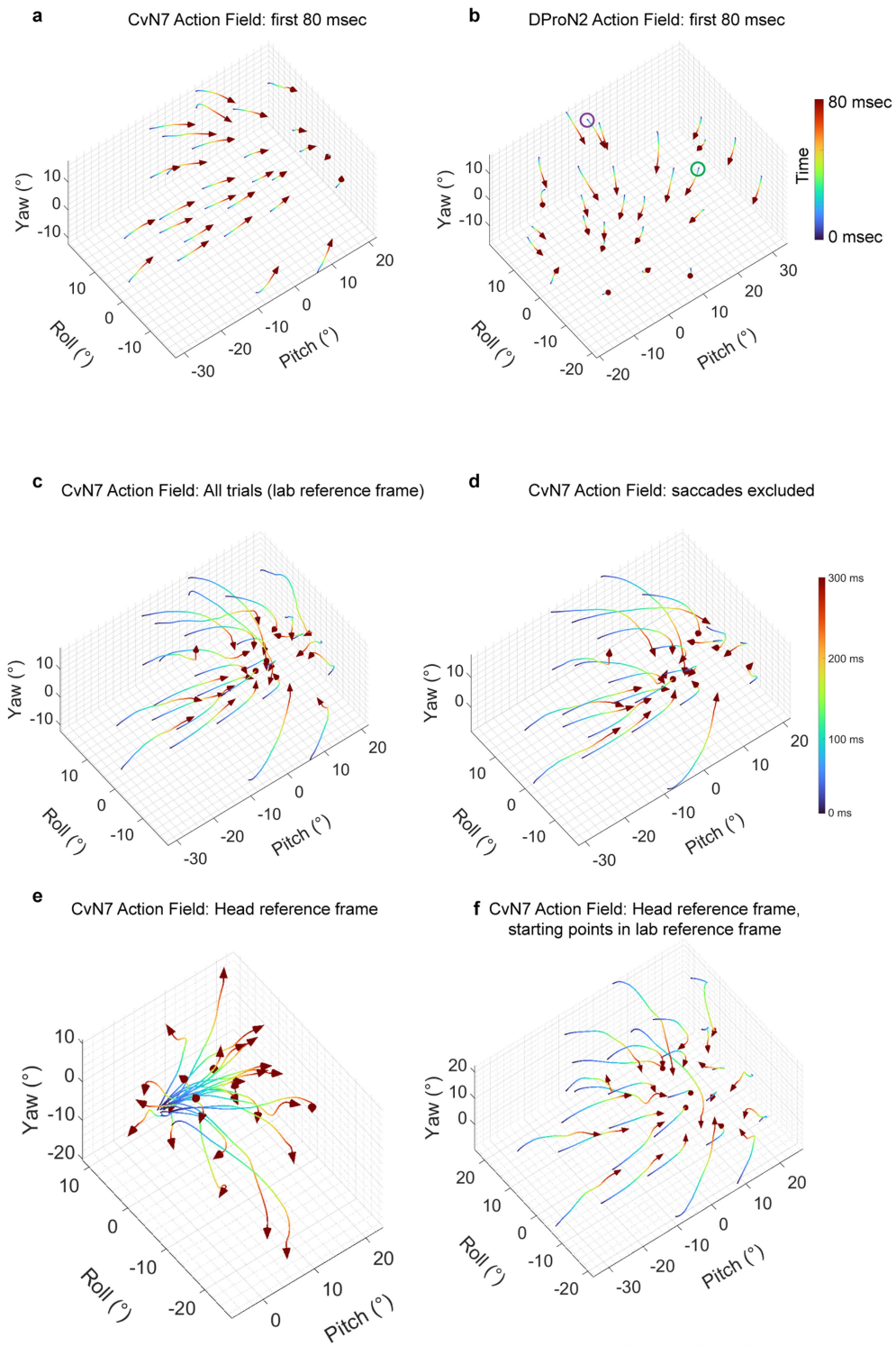
l

Yaw (°), Roll (°), Pitch (°)

Extended Data Fig. 3 | See next page for caption.

Article

Extended Data Fig. 3 | Calibration of optogenetic stimulus strength.
(a) Example trace of the membrane potential (vertical scale bar = 10 mV) of the CvN7 motor neuron in response to a 300 ms flash of 625 nm, 0.04 mW/mm^2 light. Underneath the voltage trace is a raster indicating the timing of action potentials from multiple trials. (b) An action field plotting the head movements resulting from stimulating CvN7 with the same 0.04 mW/mm^2 light pulse. (c) A plot of the 'rotational difference' between the action field in b and the equivalent data that occurs during the no-stimulus control condition – see Fig. 2a–c for more detail. (d) The neural response of CvN7 to a 0.09 mW/mm^2 stimulus. (e) The CvN7 action field resulting from a 0.09 mW/mm^2 stimulus. (f) A plot of the 'rotational difference' between the action field in e and the equivalent data that occurs during the no-stimulus control condition. (g) The neural response of CvN7 to a 0.37 mW/mm^2 stimulus. (h) The CvN7 action field resulting from a 0.37 mW/mm^2 stimulus. (i) A plot of the 'rotational difference' between the action field in h and the equivalent data that occurs during the no-stimulus control condition. (j) The neural response of CvN7 to a 1.43 mW/mm^2 stimulus. (k) The CvN7 action field resulting from a 1.43 mW/mm^2 stimulus. (l) A plot of the 'rotational difference' between the action field in k and the equivalent data that occurs during the no-stimulus control condition. Genotype for all panels: SS00754 x w +, norpA, 20XUAS-CsChrimson-mVenus (attP18).

a CvN7 Action Field: first 80 msec

b DProN2 Action Field: first 80 msec

c CvN7 Action Field: All trials (lab reference frame)

d CvN7 Action Field: saccades excluded

e CvN7 Action Field: Head reference frame

f CvN7 Action Field: Head reference frame, starting points in lab reference frame
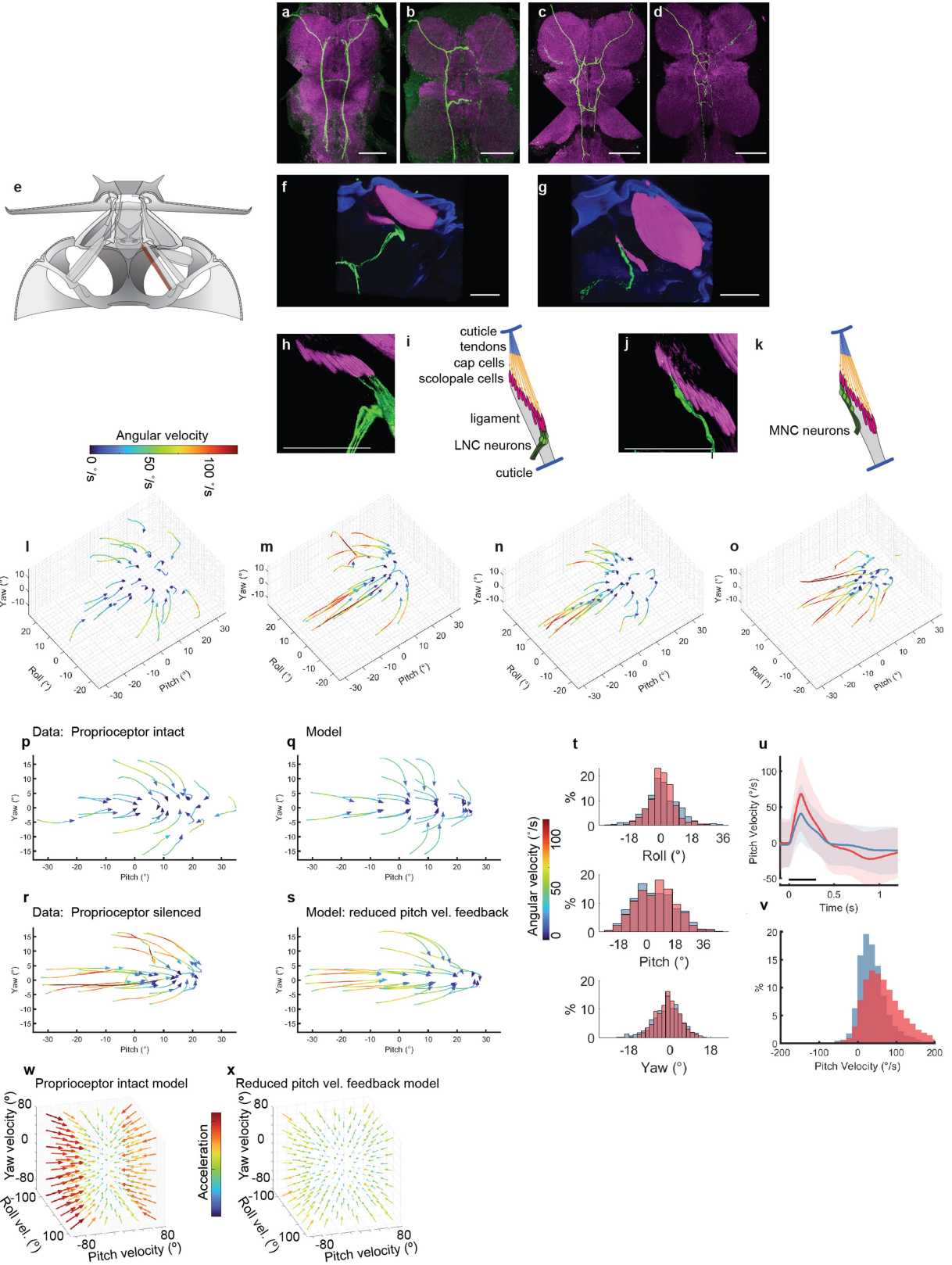
Extended Data Figure 4

Extended Data Fig. 4 | See next page for caption.

Article

Extended Data Fig. 4 | Action fields are robust to stimulation length, saccade removal and reference frame. (a-b) To confirm that the motor neuron-elicited convergence of head pose we observed is not an artefact of our 300 millisecond stimulation times, we plot just the first 80 milliseconds of the head trajectory when the angular velocity of the head is still increasing (Fig. 1h–i). (a) shows the head movements resulting from the first 80 milliseconds of CvN7 stimulation. (b) Shows the first 80 milliseconds of DProN2 stimulation. While there is, by definition, less time for the head to converge, the early head movements are still highly posture dependent and moving towards a point of convergence. Compare the different movements in the green and magenta circled trajectories in b, which are dominated by roll and pitch respectively. (c-d) To confirm that the mean head trajectories plotted in our action fields are representative of the underlying data and not biased by outlier events such as fast head saccades, we removed trials containing head saccades from the data. (c) is the action field of the CvN7 neuron replotted from Fig. 1j. (d) shows the same data but excluding any trial containing head saccades: defined as any trial containing yaw movements faster than 200 °/second. (e) All rotations in this study were measured in the lab reference frame. To confirm that the choice of reference frame did not substantially alter the results[22] we plot here the head rotations resulting from CvN7 stimulation measured in the reference frame of the head at the time of stimulus onset. By definition all head rotations start at the origin. (f) To allow comparison of the head reference frame data in e with that measured in the lab reference frame in c we moved the start points of all trajectories in e from the origin to their respective start locations in the lab frame.

a **b** **c** **d**

e

f **g**

Angular velocity

0 °/s   50 °/s   100 °/s

h **i** **j** **k**

cuticle
tendons
cap cells
scolopale cells

ligament

LNC neurons

cuticle

MNC neurons

l **m** **n** **o**

Yaw (°)
Roll (°)
Pitch (°)

Data: Proprioceptor intact

p **q** Model

Yaw (°)
Pitch (°)

r Data: Proprioceptor silenced

s Model: reduced pitch vel. feedback

Yaw (°)
Pitch (°)

t

%

Roll (°)

%

Pitch (°)

%

Yaw (°)

Angular velocity (°/s)

u

Pitch Velocity (°/s)

Time (s)

v

%

Pitch Velocity (°/s)

w Proprioceptor intact model

x Reduced pitch vel. feedback model

Yaw velocity (°)
Roll vel. (°)
Pitch velocity (°)

Acceleration

Yaw velocity (°)
Roll vel. (°)
Pitch velocity (°)

Extended Data Fig. 5 | See next page for caption.

Article

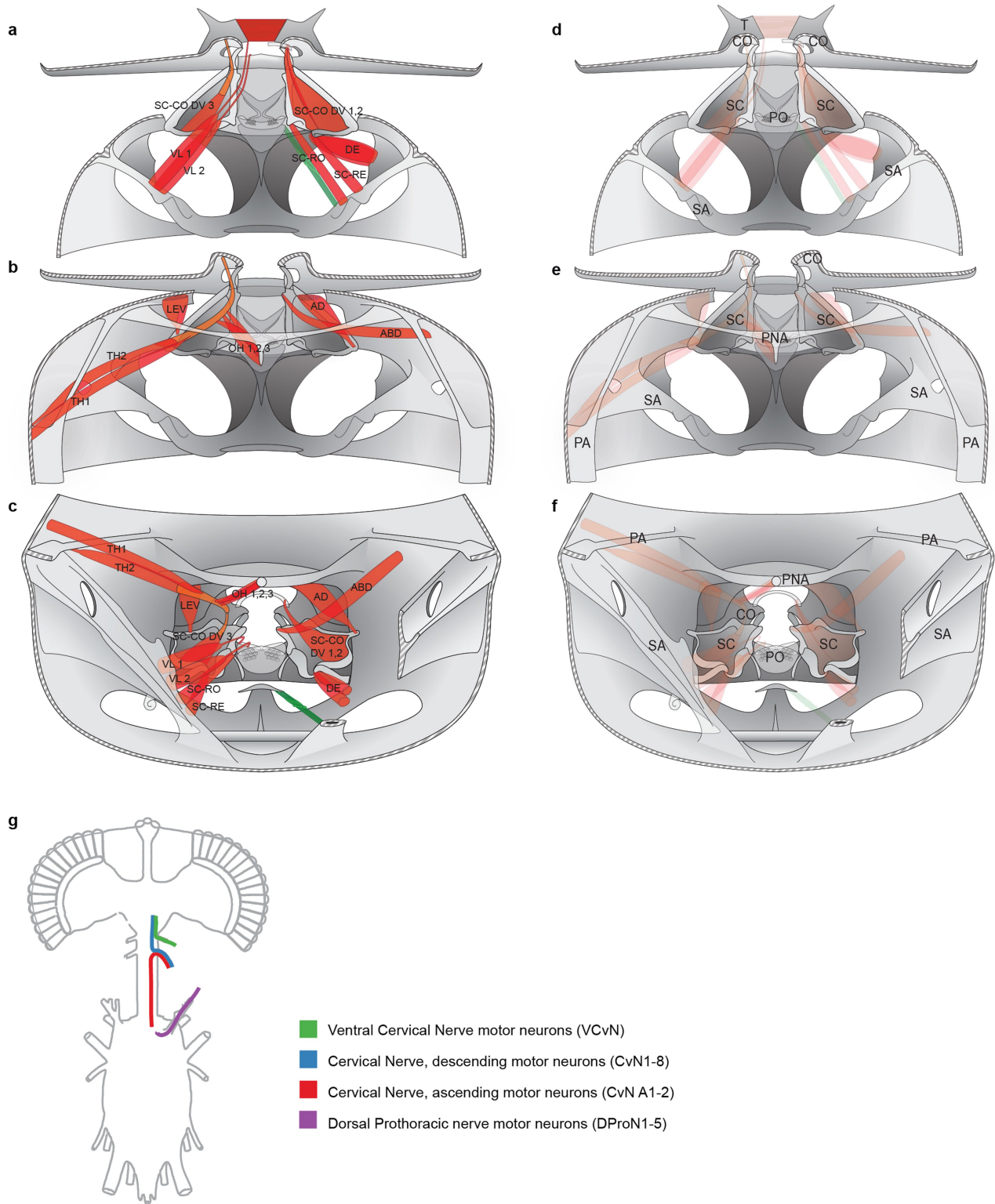**Extended Data Fig. 5 | Proprioceptive manipulations alter the action field of a motor neuron.** (a–d) central anatomy of the neck chordotonal organ afferents. (a) The central projection pattern of the Lateral Neck Chordotonal neurons (LNCs) within the ventral nerve cord. Purple: anti-BRP neuropil stain, green: anti-GFP. Genotype: JR153 x pJFRC2-10XUAS-IVS-mCD8::GFP (attP2). (b) Example of a single neuron from within the LNC population, genotype: JR153 x Multicolour flip out reporter (MCFO-1[60]). (c) The central projection pattern of the Medial Neck Chordotonal neurons (MNCs) within the ventral nerve cord. Purple: anti-BRP neuropil stain, green: anti-GFP. Genotype: JR161 x pJFRC2-10XUAS-IVS-mCD8::GFP (attP2). (d) Example of a single neuron from within the MNC population, genotype: JR161 x Multicolour flip out reporter (MCFO-1[60]). (f-k) Peripheral anatomy of the neck chordotonal afferents. (f) Peripheral expression of the same LNCs shown in (a-b). Large magenta structure: neck muscles, small magenta structure: actin rich scolopale cells of the chordotonal organ (F-actin binding Phalloidin), green: LNCs (anti-GFP). (g) Peripheral expression of the same MNCs as shown in c-d. Large magenta structure: neck muscles, small magenta structure: actin rich scolopale cells of the chordotonal organ (F-actin binding Phalloidin), green: MNCs (anti-GFP). (h) Magnification of the dendrites of the LNCs shown in f. LNC dendrites (green) can be seen to invade the magenta cylindrical scolopale cells at the lateral edge of the chordotonal organ. (i) Diagram of the chordotonal organ and the LNC neuron innervation. (j) Magnification of the dendrites of the MNCs shown in g. MNC dendrites (green) can be seen to invade the magenta cylindrical scolopale cells at the medial edge of the chordotonal organ. Scale bars in a-j are 50 μm. (k) Diagram of the chordotonal organ and the MNC neuron innervation. (l) Action field resulting from activation of the CvN7 motor neuron replotted from Fig. 3. Colour indicates the head's angular velocity. (m) Action field of the same CvN7 motor neuron when the LNCs are hyperpolarized due to expression of Kir2.1, replotted from Fig. 3. (n) Action field of the same CvN7, with the MNCs hyperpolarized due to expression of Kir2.1 (43 flies, 5160 trials, JR161 x w+ norpA, 13XLexAop2>dsFRT>CsChrimson-mVenus (attP18), BPhsFlpPest-OPt (attP3); 81B12LexAp65 (VK00022), PJFRC315-10XUAS-IVS-tdtomato::Kir2.1 (su(Hw)attp5)). (o) Action field of the same CvN7 again, with the sensory neurons of the Prosternal Organ[25] head proprioceptor hyperpolarized due to expression of Kir2.1 (12 flies, 1632 trials, SS47486 x w+ norpA, 13XLexAop2>dsFRT>CsChrimson-mVenus (attP18), BPhsFlpPest-OPt (attP3);

81B12LexAp65 (VK00022), PJFRC315-10XUAS-IVS-tdtomato::Kir2.1 (su(Hw)attp5)). (p-s) 2D plots of the same data plotted in 3D in Fig. 3g–m. (p) The CvN7 action field. Equivalent to Fig. 3g. (q) 2D plot of the results of using a feedback model to simulate the CvN7 action field. Equivalent to Fig. 3i. (r) 2D plot of the CvN7 action field when the LNC proprioceptive neurons are expressing the Kir2.1 potassium channel and thus hyperpolarized. Equivalent plot to Fig. 3k. (s) 2D plot of the CvN7 action field simulated by the same model shown in q but with the pitch velocity feedback parameter reduced to match the data in r. Equivalent plot to Fig. 3m. (t) Distributions of head rotations recorded when no stimulus was present for flies where the LNC neurons were either unperturbed (blue, empty split-Gal4 x w+ norpA, 13XLexAop2>dsFRT>CsChrimson-mVenus (attP18), BPhsFlpPest-OPt (attP3); 81B12LexAp65 (VK00022), PJFRC315-10XUAS-IVS-tdtomato::Kir2.1 (su(Hw) attp5)) or where the LNC neurons were hyperpolarized due to expression of Kir2.1 (red, JR153 x w+ norpA, 13XLexAop2>dsFRT>CsChrimson-mVenus (attP18), BPhsFlpPest-OPt (attP3); 81B12LexAp65 (VK00022), PJFRC315-10XUAS-IVS-tdtomato::Kir2.1 (su(Hw)attp5)). The mean roll, pitch and yaw head angles for control flies were 0, 8, −1° respectively with standard deviations of 8, 12, 4° (N = 36 flies). The equivalent mean values for the LNC-hyperpolarized flies were 1, 5 and 0°, with standard deviations of 9, 15 and 5 (N = 43 flies). A Two-sample Kolmogorov–Smirnov test could not reject the null hypothesis that the data from the two genotypes came from the same distribution (p-values 0.3, 0.9 and 0.2 for roll, pitch and yaw respectively, corresponding effect sizes: 0.12°, 0.09°, −0.09°). (u) Time series of the head pitch velocity during CvN7 stimulation for flies where LNC neurons were hyperpolarized due to expression of Kir2.1 (red, genotypes same as panel t) or unperturbed (blue). Shaded error bars are standard deviations, thick lines are means. Black bar indicates stimulus time course. (v) Pitch velocity distributions for LNC-hyperpolarized (red) and unperturbed (blue) flies (genotypes same as t-u). Only the velocities at the average time of peak velocity (135 ms) are plotted. (w) illustrates the velocity dependence of the model described in Fig. 2. The position dependence of the same model is shown in Fig. 2e. Arrows plot the acceleration vector that, in the absence of any stimulus, the feedback loop alone applies to the head at each velocity. (x) illustrates the same velocity dependence of the model but now for the model fit to the proprioceptor perturbed (JR153 Kir2.1) flies with reduced pitch velocity damping.
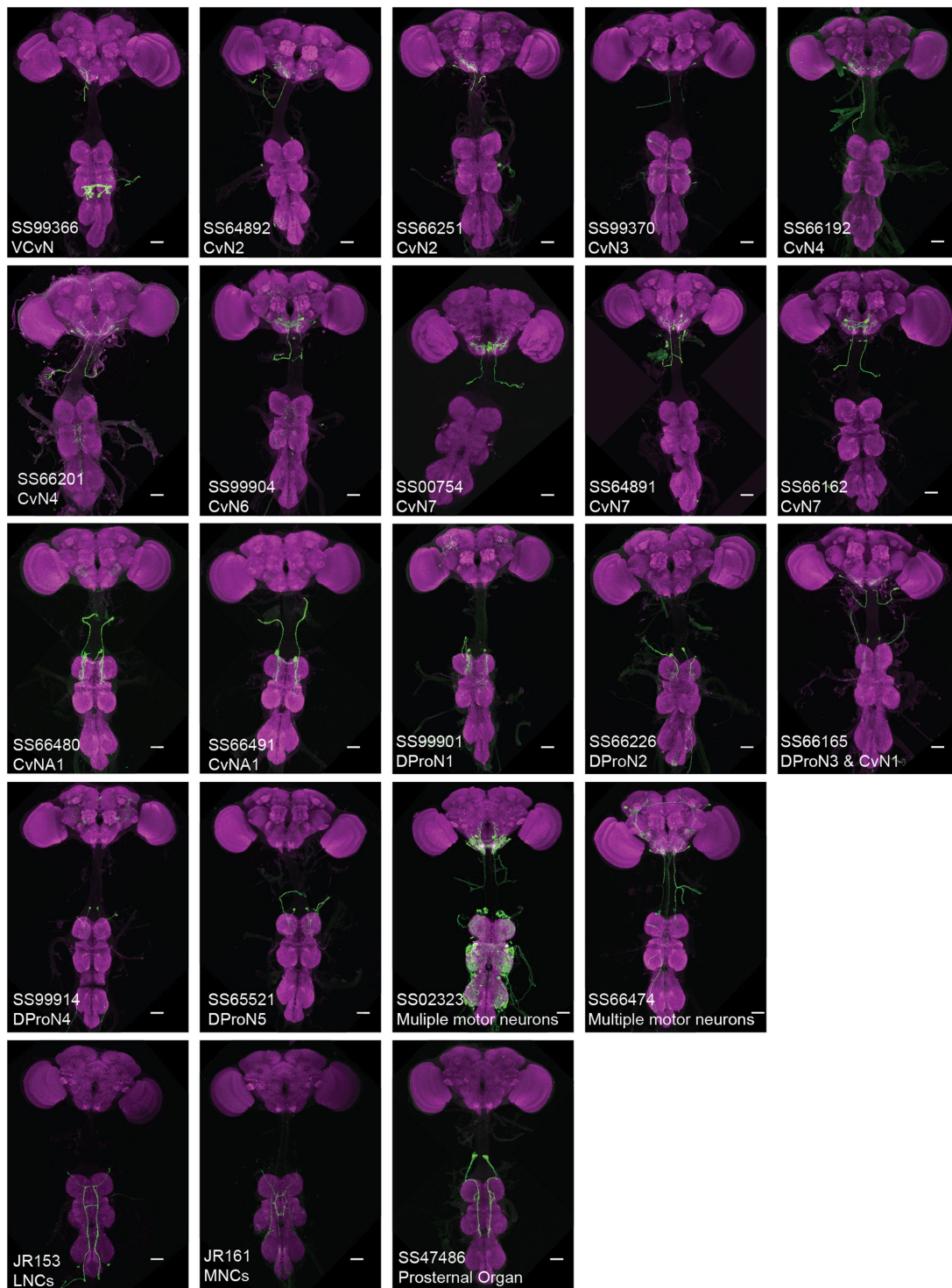
Extended Data Fig. 6 | Expression patterns of split-Gal4 stocks generated as part of this study. The full expression patterns of the split-Gal4 stocks generated and used in this study. Full stacks are available at splitgal4.janelia.org (stock names beginning "SS") and bitbucket.org/stephenhuston/code_data_ gorko_et_al (stock names beginning "JR"). A neuropil stain (anti-BRP nc82 stain) is shown in magenta. The expression of each stock when crossed to UAS-CsChrimson-mVenus (20XUAS-CsChrimson-mVenus(attP18)) is shown in green (anti-GFP stain). Scale bars = 50 μm.

Ventral Cervical Nerve motor neurons (VCvN)

Cervical Nerve, descending motor neurons (CvN1-8)

Cervical Nerve, ascending motor neurons (CvN A1-2)

Dorsal Prothoracic nerve motor neurons (DProN1-5)

Extended Data Fig. 7 | See next page for caption.

Extended Data Fig. 7 | Neck musculature and nerves of *Drosophila melanogaster.* (a-c) Diagrams of the fly's neck muscles. Grey = cuticle, red = muscle, orange = tendon, green = neck chordotonal organ. (a) A ventral slice through the fly's neck, horizontal plane viewed from above. (b) Dorsal slice through the fly's neck. (c) View of the same muscles in a-b from inside the fly's thorax, facing towards the neck. SC-CO DV - dorsoventral muscles linking the cervical sclerite and the condyle. VL – ventral longitudinal muscles, DE - depressor muscles, SC-RO – sclerite rotator muscle, SC-RE - sclerite retractor muscle, LEV - levator muscle, TH - transverse horizontal muscles, OH - oblique horizontal muscles, AD - adductor muscle, ABD - abductor muscle. (d-f) Diagrams of the major cuticular structures within the fly's neck. Grey= cuticle, transparent red = muscles, transparent green = chordotonal organ. (d) Ventral slice through the fly's neck, (e) Dorsal slice through the fly's neck, (f) view from inside the fly's prothorax, facing towards the neck. T - tentorium, CO - condyle, SC – cervical sclerite, PO – prosternal organ, SA – sternal apodeme, PNA – pronotal apodeme, PA – pleuron apodem. Muscle and cuticle structure are named in a way that attempts to match, where possible, the terminology of Strausfeld[9]. (g) Diagram of the four neck motor outputs of the fly central nervous system after which we have named the motor neurons. CNS outline adapted from[11]. VCvN motor neurons exit through the Ventral Cervical Nerve (green) that branches from the subesophageal zone where it meets the cervical connective (called the VCN in Strausfeld[9]). DProN motor neurons exit the ventral nerve cord through the Dorsal Prothoracic nerve (purple, called frontal nerve/FN in Strausfeld[9]). CvN motor neurons exit through Cervical Nerve (blue, called CN in Strausfeld[9]), which branches from the cervical connective half way down its length. The CvN **A**1 and CvN **A**2 motor neurons (red) have the letter A before the neuron number to indicate that they ascend from the ventral nerve cord to reach the Cervical nerve, in contrast to the majority of CvN neurons which descend from the subesophageal zone. CvN A1-2 are likely homologous to ADN1-2 in the blowfly[9] which, in the blowfly, exit from their own thin nerve that originates in the ventral nerve cord. In *Drosophila melanogaster* this nerve is missing and appears to be fused with the cervical connective and the Cervical Nerve to allow CvN A1-2 to exit the central nervous system via the Cervical Nerve.
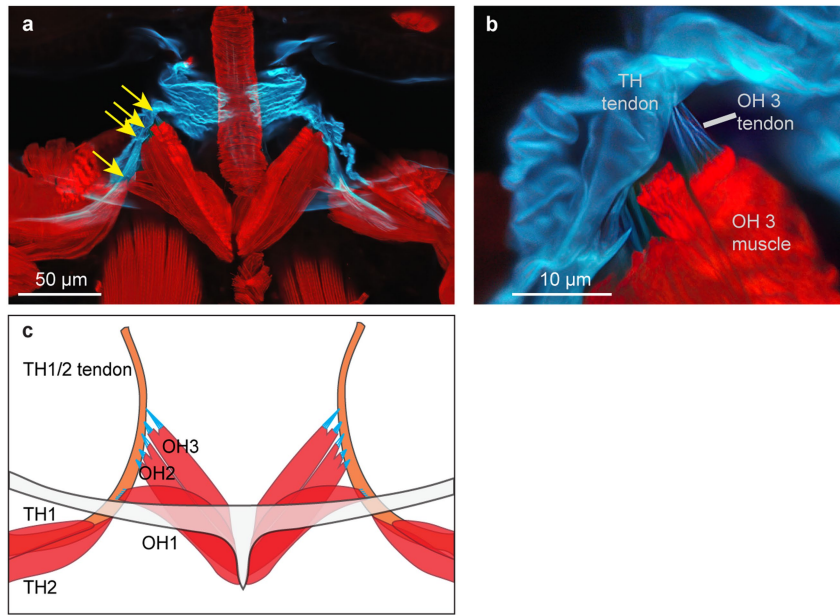
Extended Data Fig. 8 | The tendons of yaw muscles are coupled. (a) Confocal image of the dorsal neck musculature showing the OH muscles and the large, curved tendon of the TH muscles. Red = muscles (F-actin stained with Phalloidin), blue = tendons and cuticle (chitin binding Calcofluor White). Yellow arrows indicate points of coupling between the OH and TH tendons. The three small OH muscles originate from the midline and travel anterolaterally to where they connect to the large, curved TH tendon via small tendon tendrils. (b) shows a higher magnification of the coupling between the OH 3 muscle's tendon and that of the TH muscle. (c) Diagram of the image in a. Muscles are shown in red, the TH muscle tendon is shown in orange and the OH muscle tendons are shown in blue. Such an arrangement is likely to allow the OH muscles to change the line of action of the TH muscle by altering its tendon's geometry. Such inter-muscle interactions will not be captured by our linear model.

Extended Data Table 1 | Genotypes for flies used in each figure panel

Figure	Genotype (see Supplemental Table 1 for full genotypes)	Age (days)
1b	HAV5(double Label);SS00754(CvN7) x R21H04-LexA(LPTCs)	2-3
1c-e	CvN7-GFP	3-4
1g	SS00754(CvN7) x Flp-CsChr	5
1h-j	SS00754(CvN7) x CsChr	5
1k	SS02323(multiNMN) x Flp-CsChr	5
2a-c	SS00754(CvN7) X CsChr	5
3a-b	JR153(LNC) X pJFRC2-GFP	3
3d-e	JR161(MNC) X pJFRC2-GFP	6
3g-h	Empty split-GAL4 X CvN7-CsChr; UAS-Kir2.1	3
3k-l	JR153(LNC) X CvN7-CsChr; UAS-Kir2.1	3
4a-b	Multiple split-Gal4 stocks X Flp-CsChr	5
4c,e	SS00754(CvN7) X pJFRC2-GFP	3-4
4i-j	Multiple split-Gal4 stocks X Flp-CsChr	5

Genotypes and ages of the flies used to generate the data in each of the figure panels listed in the leftmost column. Genotypes are described using the identifiers from Supplementary Table 1. For the full genotype and source corresponding to each identifier, see Supplementary Table 1.

nature portfolio

Corresponding author(s):   Stephen Huston

Last updated by author(s):   4th Oct 2023

Reporting Summary

Nature Portfolio wishes to improve the reproducibility of the work that we publish. This form provides structure for consistency and transparency in reporting. For further information on Nature Portfolio policies, see our Editorial Policies and the Editorial Policy Checklist.

Statistics

For all statistical analyses, confirm that the following items are present in the figure legend, table legend, main text, or Methods section.

n/a	Confirmed	
☐	☒	The exact sample size (*n*) for each experimental group/condition, given as a discrete number and unit of measurement
☐	☒	A statement on whether measurements were taken from distinct samples or whether the same sample was measured repeatedly
☐	☒	The statistical test(s) used AND whether they are one- or two-sided *Only common tests should be described solely by name; describe more complex techniques in the Methods section.*
☒	☐	A description of all covariates tested
☐	☒	A description of any assumptions or corrections, such as tests of normality and adjustment for multiple comparisons
☐	☒	A full description of the statistical parameters including central tendency (e.g. means) or other basic estimates (e.g. regression coefficient) AND variation (e.g. standard deviation) or associated estimates of uncertainty (e.g. confidence intervals)
☐	☒	For null hypothesis testing, the test statistic (e.g. *F*, *t*, *r*) with confidence intervals, effect sizes, degrees of freedom and *P* value noted *Give P values as exact values whenever suitable.*
☒	☐	For Bayesian analysis, information on the choice of priors and Markov chain Monte Carlo settings
☒	☐	For hierarchical and complex designs, identification of the appropriate level for tests and full reporting of outcomes
☐	☒	Estimates of effect sizes (e.g. Cohen's *d*, Pearson's *r*), indicating how they were calculated

Our web collection on statistics for biologists contains articles on many of the points above.

Software and code

Policy information about availability of computer code

Data collection	Matlab
Data analysis	Code to reproduce the figures in this paper is available at bitbucket.org/stephenhuston/code_data_gorko_et_al. https://github.com/allenleetc/orthocam commit 15beb01 Matlab R2022a Matlab System Identification Toolbox Version 9.16 Matlab Signal Processing Toolbox Version 9.0 Matlab Statistics and Machine Learning Toolbox Version 12.3 Matlab Curve Fitting Toolbox Version 3.7 http://msl.cs.uiuc.edu/~yershova/software/so3sampling/so3sampling.htm https://github.com/mattools/matGeom commit 4a7b48b

For manuscripts utilizing custom algorithms or software that are central to the research but not yet described in published literature, software must be made available to editors and reviewers. We strongly encourage code deposition in a community repository (e.g. GitHub). See the Nature Portfolio guidelines for submitting code & software for further information.

Data

All manuscripts must include a data availability statement. This statement should provide the following information, where applicable:

- Accession codes, unique identifiers, or web links for publicly available datasets
- A description of any restrictions on data availability
- For clinical datasets or third party data, please ensure that the statement adheres to our policy

Data to reproduce the figures in this paper are available at bitbucket.org/stephenhuston/code_data_gorko_et_al. The expression patterns and flies for split-gal4 lines generated in this study are available online at splitgal4.janelia.org (release: "Gorko et al 2024"), except for JR153 and JR161 whose expression patterns can be downloaded at bitbucket.org/stephenhuston/code_data_gorko_et_al, flies available upon request.   Electron Microscopy data is available at fafb.catmaid.virtualflybrain.org (SKIDs: 1167858 (CvN6), 1337777 (CvN7)).

Research involving human participants, their data, or biological material

Policy information about studies with human participants or human data. See also policy information about sex, gender (identity/presentation), and sexual orientation and race, ethnicity and racism.

Reporting on sex and gender	N/A
Reporting on race, ethnicity, or other socially relevant groupings	N/A
Population characteristics	N/A
Recruitment	N/A
Ethics oversight	N/A

Note that full information on the approval of the study protocol must also be provided in the manuscript.

Field-specific reporting

Please select the one below that is the best fit for your research. If you are not sure, read the appropriate sections before making your selection.

☒ Life sciences ☐ Behavioural & social sciences ☐ Ecological, evolutionary & environmental sciences

For a reference copy of the document with all sections, see nature.com/documents/nr-reporting-summary-flat.pdf

Life sciences study design

All studies must disclose on these points even when the disclosure is negative.

Sample size	All initial sample sizes were chosen based on conventional standards used in our field and predicted animal-to-animal variability. Sample sizes were increased until all starting head position bins within each 'action map' contained at least 4 trials each.
Data exclusions	Data were included or excluded from behavioral data sets based upon CsChrimson-mVenus expression in each individual fly's brain after post-experiment dissection. See supplemental methods for details.
Replication	Findings were replicated across multiple animals, multiple genotypes and multiple different neuron types. Replicates varied in number between experiments and are specified in the figure legends. They ranged from 21-43 flies and 2132-3912 trials.
Randomization	Behavioral experiments were performed blind to the identity of any stimulated neuron (see below) and thus randomized by nature of the experimental design. For model fitting and validation, data was assigned to the fitting or validation data set pseudo-randomnly using the Matlab rand() function.
Blinding	When using the stochastic flp-out technique, behavioral experiments were performed blind to the neuron that expressed CsChrimson-mVenus and was thus stimulated in each animal. The information only became available 1-2 weeks after the experiment once the nervous system had been imaged.

Reporting for specific materials, systems and methods

We require information from authors about some types of materials, experimental systems and methods used in many studies. Here, indicate whether each material, system or method listed is relevant to your study. If you are not sure if a list item applies to your research, read the appropriate section before selecting a response.

Materials & experimental systems

n/a	Involved in the study
☐	☒ Antibodies
☒	☐ Eukaryotic cell lines
☒	☐ Palaeontology and archaeology
☐	☒ Animals and other organisms
☒	☐ Clinical data
☒	☐ Dual use research of concern
☒	☐ Plants

Methods

n/a	Involved in the study
☒	☐ ChIP-seq
☒	☐ Flow cytometry
☒	☐ MRI-based neuroimaging

Antibodies

Antibodies used	To visualize mVenus expression and assess relative expression levels among flies, an anti-GFP antibody directly conjugated to Alexa Fluor® 488 was used (Thermo Fisher Scientific A-21311, 1:500). The neuropil was labeled by incubation with mouse anti-BRP hybridoma supernatant (nc82, Developmental Studies Hybridoma Bank, Univ. Iowa, 1:30; concomitantly with anti-GFP), followed by an Alexa Fluor® 568-conjugated goat anti-mouse antibody (ThermoFisher Scientific A-11031, 1:400). In experiments with flies expressing both GFP and tdTomato, the latter was detected by adding rat monoclonal anti-RFP antibody (5F8, Chromotek, 1:500) followed by CyTM3-conjugated goat anti-rabbit antibody (Jackson ImmunoResearch 111-165-144, 1:500). Here, the anti-BRP antibody was detected by a CyTM5-conjugated goat anti-mouse secondary antibody (Jackson ImmunoResearch 115-175-166, 1:500).
Validation	The rabbit anti-GFP antibody A-21311 (ThermoFisher Scientific) is an Alexa Fluor® 488 conjugate of antibody A-21311 (ThermoFisher Scientific). Together these antibodies have been used for immunohistochemistry in at least 949 publications according to the manufacturer's website, including studies of many different split GAL4 lines cited on https://splitgal4.janelia.org/cgi-bin/splitgal4.cgi. Our work further confirms the specificity of the antibody to GFP since it labels selectively neurons that genetically express GFP. Similarly, the rat monoclonal anti-RFP antibody 5F8 (Chromotek) selectively labels tdTomato expressing neurons in transgenic flies (our study), and it has been used in at least 315 previous published studies for IHC and other applications. The manufacturer validated the specificity in immunofluorescence studies using transfected HeLa cells expressing a tdTomato tagged protein in the Golgi apparatus. Monoclonal antibody nc82 to the Bruchpilot protein in presynaptic active zones is the current gold standard to label Drosophila synapses. It has been validated by the hybridoma bank depositor for immunohistochemistry (see Wagh et al. 10.1016/j.neuron.2006.02.008). Of note, this antibody is fixation-sensitive, i.e., strong/denaturing fixation conditions (such as >2% PFA for >1 h at room temperature) yield a poor signal.

Animals and other research organisms

Policy information about studies involving animals; ARRIVE guidelines recommended for reporting animal research, and Sex and Gender in Research

Laboratory animals	Drosophila melanogaster. See supplemental tables 1-2 for detailed strain/genotype/age information.
Wild animals	Study did not involve wild animals.
Reporting on sex	Study was performed only on males due to constraints in stock construction.
Field-collected samples	No field collected samples used.
Ethics oversight	No ethical approval was required because experiments were performed on Drosophila melanogaster.

Note that full information on the approval of the study protocol must also be provided in the manuscript.